Volume 1, Issue 1, May 2025

International Journal of Energy Efficiency Engineering (IJEEE)

EDITOR-IN-CHIEF:
Ethan Languri, PhD

https://publish.tntech.edu/index.php/IJEEE

INTERNATIONAL JOURNAL OF
ENERGY EFFICIENCY ENGINEERING

Table of Contents

International Journal of Energy Efficiency Engineering
Volume 1, Issue 1 — Spring 2025

INTERNATIONAL JOURNAL OF
ENERGY EFFICIENCY ENGINEERING

From the Editor-in-Chief

Welcome to the inaugural issue of the *International Journal of Energy Efficiency Engineering (IJEEE)*, published in May 2025. In this issue, we present original and peer-reviewed research with an emphasis on energy efficiency and engineering using artificial intelligence (AI), experimental, numerical, and theoretical methods. These papers cover areas in building energy, materials, industrial equipment and process, and finally fuel production.

These contributions reflect the IJEEE's commitment to bridging academic research and industrial innovation, focusing on quality research with direct impact in industry.

We sincerely thank our authors, reviewers, and editorial team for their valuable contribution and dedication. We hope this issue inspires further dialogue towards smarter and more efficient energy systems.

Sincerely,

Dr. Ethan Mohseni Languri, PhD, PE
Editor-in-Chief, IJEEE
elanguri@tntech.edu
+1 (931) 372-6790
Website: https://publish.tntech.edu/index.php/IJEEE

International Journal of Energy Efficiency Engineering (IJEEE)
Volume 1, Issue 1 (May 2025), Pages 1-4

INTERNATIONAL JOURNAL OF
ENERGY EFFICIENCY ENGINEERING

Letter to the Editor

Glenn T. Cunningham, PhD, P.E.

The question is sometimes raised as to whether manufacturing companies should be concerned with energy efficiency and even be committed to establishing and maintaining energy efficiency programs. When looking at the general financial landscape of an industrial company there are three main costs to be managed. These are raw materials, labor and energy. Managing the use of materials needed to produce a product is almost always done well because if this is not, the company cannot long exist. Companies naturally do a pretty good job managing labor. If there are not enough employees, production levels cannot be maintained. Being overstaffed typically does not occur for long periods of time. So, the last area where major cost savings are possible is energy. With rising prices for natural gas, oil, electricity and other energy sources ignoring energy management can deliver a major financial hit to the bottom line.

In a world where tracking and reducing carbon emissions is becoming the rule instead of the exception, managing energy use is the key factor. In Europe a metric ton (MT) of carbon has an actual value of between $75 to $100 per MT, US $. The US does not currently have a carbon tax even though States like California and Washington and the northeastern states do have cap-and-trade programs. Generally speaking, the cost of carbon emissions, both in the US and Europe appear to be headed higher in the coming years. Any competent management team must have a plan to address this growing cost.

How should a company think about organizing its energy management activities? A good place to start is to research the energy management standard ISO-50001. This standard lays out in detail how to establish and run an effective energy management program. While many companies decide not to formally pursue obtaining ISO-50001 certification, studying the

recommended structure and activities can lead to the implementation of an effective program. There is also ISO-50001 Ready, which is designed to get a company started in developing an energy management program along the lines of the full ISO-50001 standard. It is sometimes called ISO-50001 Light. This can be a good starting point. The US DOE and US EPA also have voluntary no cost programs to support energy efficiency programs.

After years of working with companies on energy management there are some important items that should not be ignored. Some of these will be listed and discussed. These are not necessarily in any particular order or order of importance. It is not meant to be an all-inclusive list.

- Upper Management must be committed and involved is the energy efficiency program. When an assessment or Treasure Hunt starts at a manufacturing facility having the plant manager or someone even higher up the corporate chain of command attend the kick-off meeting and say how important the activity is to the success of the company makes a world of difference. It sets a tone for the program and the event.
- Each plant should have an energy champion and a significant portion of their job be dedicated to running the energy program. You cannot just add this responsibility to someone who already has a full plate of responsibilities.
- Each plant should have an energy management committee made up of representatives from engineering, maintenance, accounting, health & safety and management. This committee must meet at least monthly to identify and promote potential efficiency projects, work for their implementation and discuss other energy-related issues.
- Plant representatives should have a relationship with the local utility and generating companies providing energy to the plant. Several times per year the plant should have their company representatives from the utility companies into the plant to discuss issues with the service and any programs the utility might have that could benefit the company. Somes there are rebate programs the company never knows about and fail to participate in. The utility rate structure should be thoroughly understood by multiple employees at the plant. Issues like electrical demand, power factor, time-of-use rates, interruptible rates, etc. must be thoroughly understood at the plant.
- The Energy Committee should run a suggestion/reward program for employees at the plant. A suggestion box should be established where all employees can suggest projects

or changes in procedures to save energy or make other improvements. Once or twice a year energy program should give an award for the best suggestion made during the last period of time. An annual award like a long weekend trip to a resort will keep the participation rate high.

- Give out tee shirts, hard hat stickers, etc. publicizing the program.
- Allocate a pool of funds annually to pay for energy efficiency projects.
- For multinational companies, if plants where there is no carbon tax must compete for funding for projects with plants located where there is a carbon tax, allow both to claim the value of reduced emissions at the same carbon value in payback calculations. If the plants without a carbon tax cannot include the carbon value in their calculations, they cannot compete with the other plants and will receive little or no support for energy projects.
- Annually, hold a corporate meeting of all the energy managers and teams where they can present about successful projects and spread the word so these ideas can be implemented across the company.
- Hire a corporate energy manager to communicate with all the plants to help organize and run the energy efficiency program.
- Have members of the most successful plant programs visit other plants to share their projects and other secrets of their success.
- Have weekly video meetings where ideas are exchanged, and plants make suggestions for each other.
- Encourage each plant to hold at least one energy Treasure Hunt each year. The first of these may require assistance from outside experienced personnel, but after one or two the plant can support this activity internally.
- Participate in US DOE energy conservation programs and utilize the resources DOE has to support the energy efficiency program.
- Apply for awards and recognition for the program's successes. Publicize the successes of the program.

- "You cannot Manage what you do not Measure." Develop an ability to obtain the measurements necessary to accurately quantify savings for suggested energy saving projects.
- Plant managers should have energy performance as one of the deciding factors in determining the amount of their annual bonus. In fact, all employees who receive performance bonuses should have energy performance as one of the deciding criteria.

Establishing an energy management program with the characteristics mentioned above will foster an environment within the corporation where energy efficiency and environmental stewardship can flourish. New employees must be trained in how the program is organized and functions to assure it continues and grows into the future.

Author Biography

Dr. Glenn T. Cunningham has taught mechanical engineering courses at Tennessee Tech University since 1986 and is the former director of the Industrial Assessment Center, which has provided over 230 energy assessments for small to medium sized industries funded by the U.S. Department of Energy (DOE). Dr. Cunningham has been involved in performing assessments for over 35 years for a wide variety of clients. Dr. Cunningham holds the following licenses and certifications: Fellow of the American Society of Mechanical Engineers; Certified Practitioner in Energy Management Systems, and Registered Professional Engineer in Tennessee and Kentucky.

International Journal of Energy Efficiency Engineering (IJEEE)
Volume 1, Issue 1 (May 2025), Pages 5-26

INTERNATIONAL JOURNAL OF
ENERGY EFFICIENCY ENGINEERING

Predicting Energy Consumption in Buildings Using Various Artificial Intelligence Models

Yazeed E. AbuShanab, Mohamed I Youssef, Omar Shaker, M Abdelaziz Youssef, Ryoichi S Amano[1]

Department of Mechanical Engineering, University of Wisconsin-Milwaukee 115 E. Reindl Way, Glendale, WI 53212

Abstract

Accurately predicting energy consumption in buildings is vital for optimizing energy efficiency, reducing costs, and supporting sustainability efforts. This study uses a dataset that spans and broadcasts hourly energy consumption for a specific building in Spain, using a dataset spanning an entire year. The dataset includes hourly energy usage in kilowatt-hours (kWh) and features representing environmental conditions, including temperature, humidity, and precipitation. alongside time-related variables, including the hour of the day, day of the week, and seasonal markers. These features provide a detailed view of how internal and external conditions influence energy usage patterns. Data preprocessing included handling missing values, feature selection, and engineering temporal variables such as Hour, Day of Year, and Is Weekend, which capture essential behavioral and operational dynamics. The building analyzed is a representative structure with typical heating, ventilation, and air conditioning (HVAC) systems. This model is well-suited for analyzing energy consumption patterns across different environmental and operational conditions. Various regression models were applied, including Linear Regression, Ridge and Lasso Regression, Support Vector Regression (SVR), K-

[1] Corresponding Author: Professor Ryoichi Amano, amano@uwm.edu

Nearest Neighbors (KNN), Random Forest, XGBoost, and Neural Networks. Model performance was assessed using Mean Absolute Error (MAE) and R-squared (R^2) metrics. Random Forest emerged as the best-performing model, achieving an MAE of 8.33 and an R^2 of 0.954, highlighting its strong ability to capture the building's energy consumption patterns. This research highlights the potential of regression models and artificial intelligence in improving energy forecasting, serving as a foundation for advancing building energy management systems.

Keywords: *Energy Consumption in Buildings; Energy Forecasting; Artificial Intelligence; Annual Energy Savings; Linear Regression; Ridge and Lasso Regression; Support Vector Regression (SVR); K-Nearest Neighbors (KNN); Random Forest, XGBoost, and Neural Networks.*

I. INTRODUCTION

Nowadays, it is impossible to overlook the changes and oscillations in the energy industry. Considering the duty of maintaining and optimizing the current sources and emphasizing the significance of energy management throughout the entire system life cycle with all of their methodologies and techniques, it also became clear that there is a significant demand for dependable yet sustainable energy resources. Closing the gap and developing reliable substitutes for such systems are necessary to address this weakness. As mentioned earlier, resource allocation, expenditure optimization, and comprehensive but meticulous design objectively relate to and significantly impact the need. Key elements of any organization's success and operations are the efficiency of resource management, energy optimization, and continuous process improvement procedures, which start with identifying, evaluating, and responding to steps for improving the current procedure or process and conclude with the steps of documenting and recording them for future reference [1] [2].

Driven by increasing energy demands, the need to minimize greenhouse gas emissions, and governmental policies encouraging energy efficiency, smart energy systems have emerged as an effective solution for optimizing energy consumption and promoting sustainability. These

systems offer the potential to mitigate the environmental impact of rising energy use due to urbanization, industrialization, and population growth by reducing pollution and greenhouse gases while conserving resources through intelligent analysis of energy consumption patterns and identification of opportunities for waste reduction [3].

As energy efficiency becomes increasingly important in mitigating climate change and reducing operational costs, developing predictive tools to optimize energy consumption aligns with personal and professional goals. This research study uses machine learning techniques to predict hourly energy consumption in buildings. By analyzing weather and temporal features, such as temperature, humidity, and time of day, the aim is to develop accurate predictive models for optimizing energy management. This research paper compares the performance of various models, including Random Forest, Ridge Regression, and Neural Networks, to identify the most effective approach for this task. In addition to its relevance to sustainability and energy management, it also serves as a valuable application of machine learning techniques in such fields, bridging theory with a real-world problem.

Several models were evaluated to predict energy consumption, each chosen for its unique strengths in handling different aspects of the data. Random Forest (RF) was evaluated due to its ability to handle non-linear relationships and complex data interactions, which are common in energy consumption patterns. As an ensemble method, RF also reduces the risk of overfitting and is robust in dealing with missing data. Linear models, while simpler and more interpretable, were evaluated to provide a baseline for comparison, although they failed to capture the non-linear complexities of the energy consumption data effectively. Support Vector Regression (SVR) was included for its ability to handle high-dimensional spaces and its success in other regression tasks, but it struggled with the non-linearities in the dataset, leading to poorer performance than RF. Other models were considered to benchmark the performance of more sophisticated algorithms. Furthermore, Neural Networks were also evaluated, as they are known for their powerful capability to model complex, non-linear relationships. However, Neural Networks might not be required for the model because the model might not be as complex to handle using Neural Networks.

The main issues in energy consumption analysis are examined in this study, emphasizing anomaly

detection, model performance, and feature relevance. It seeks to pinpoint the most significant variables that affect energy use, such as weather and seasonal trends. It also compares several machine learning models to see which provides the optimum accuracy and interpretability balance. Identifying anomalies or outliers in odd usage patterns is another crucial component of improving energy management. By tackling these issues, the research paper aims to show how machine learning can be used in the real world and offer practical insights for enhancing building operations' energy efficiency.

II. LITERATURE REVIEW

In intelligent energy systems, the quick development of artificial intelligence (AI) algorithms has created new chances to optimize energy use and encourage sustainable habits. To support load balancing, demand side management, and power grid stability optimization calculations, artificial intelligence algorithms can examine user behavior and energy usage trends. In the end, these algorithms can offer energy-saving measures. To solve the increasing issues of energy consumption, environmental sustainability, and resource efficiency, energy efficiency is essential.

The primary goal of univariate regression is to examine the relationship between a dependent variable and a single independent variable, establishing a linear equation that represents the connection between the two models; multilinear Regression is the term for regression models that have one dependent variable and multiple independent variables. Regression analysis is a statistical technique for predicting the relationship between variables with reason and result relationships [4].

Additionally, this can be used as a basis for future studies on the estimation and forecasting of energy use in the food and beverage business, with the results and conclusions being used in a multi-criteria decision-making process, such as the PROMETHEE model, to forecast the behavior of that industry [5]. To classify data (classification) and forecast continuous values (Regression), the Random Forest regression technique first creates several datasets by resampling the original data. As shown in [6], this sampling strategy is commonly used for both small and big population selection. A decision tree is built for these resampled datasets without pruning. One important characteristic of random forests is that, instead of assessing every predictor, a random subset of

the available predictor variables is considered for the optimum split at each decision-making step. After this set of trees is created, the forecasts from each tree are combined to create predictions on fresh data. For regression tasks, this aggregation entails averaging the predictions, and for classification problems, a majority vote. Standard bagging can be seen as a special case of Random Forests where all predictors are considered at each split rather than a random subset [7].

Regression techniques like Lasso and Ridge work well for managing multicollinearity and avoiding overfitting. Multicollinearity and automated model selection benefit from Lasso (L1 regularization), which encourages simpler models with fewer parameters. Ridge regression (L2 regularization), especially well-suited for multicollinearity, lowers estimate bias and variability. The nature of the issue and the intended model attributes determine which of the Lasso and Ridge regression is best. Ridge regression works well when every feature affects performance, but Lasso is best suited for many characteristics with few significant ones. These methods help improve model performance and interpretability, which helps researchers create dependable regression models for various uses. When trying to figure out how best to use each element in a statistical model to predict or comprehend the response variable, multicollinearity can provide skewed or misleading findings [8]. Additionally, it may lead to less dependable results and broader confidence ranges. The particulars of the problem and the intended model attributes determine which of Lasso and Ridge regression is best. Lasso works well when there are many characteristics, but only a few are significant. Ridge regression, on the other hand, works well when multicollinearity is present and every feature affects the model's performance. Both strategies provide strong frameworks for improving models [9].

Support Vector Machines (SVM) is a learning method implemented using SVM, which helps identify minute patterns in large, complicated data sets. The system uses discriminative categorization learning as an example to forecast the classes of previously unknown data. It's based on learning machines that apply the inductive concept of structural risk reduction to achieve good generalization on a small set of learning patterns. Support Vector Regression (SVR) aims to achieve generalized performance by reducing the generalization error bound rather than the observed training error [10]. The concept behind Support Vector Regression (SVR) is to compute a linear regression function in a high-dimensional feature space, where a nonlinear function maps the input data into this space. The approximation of difficult engineering studies, convex

quadratic programming, loss function selection, time series and financial (noisy and risky) prediction, and other areas have all used SVR. In this study, an attempt has been made to discuss the current theory, procedures, new advancements, and applications of SVR [11].

Unlabeled observations are categorized using the K-nearest Neighbors (kNN) classifier by placing them in the same class as the most comparable labeled samples. Both the training and test datasets observational characteristics are gathered [12].
The kNN algorithm's diagnostic performance is greatly impacted by the choice of k. Although a large k lessens the effect of variation by random error, it also increases the possibility of overlooking a subtle but significant pattern. Finding a balance between overfitting and underfitting is crucial when selecting a k value [13].

Neural networks are inspired by the brain's structure for information processing. While they do not perfectly replicate the brain's functions, they are scientifically motivated models. Due to their ability to learn from data, neural networks have proven to be highly effective in various forecasting and business classification applications [14]. To effectively complete a job, the artificial neural network learns by adjusting the weights in the network design. It may automatically learn from examples or input-output relationships, or it can learn from existing training patterns. Despite their continued remarkable performance on well-known machine learning challenges, it has been challenging to prove that neural network models can reason about ideas [15] [16]. Artificial intelligence (AI) techniques are applied in many study domains, including material strength and properties, healthcare, risk assessment and prediction, soil mechanics and characteristics, and building energy consumption [17].

III. METHODOLOGY

A. Study Limitations

This study focuses on a residential facility with a moderate electricity consumption load compared to industrial and commercial buildings. One limitation is its geographical scope, as the research was conducted on a building in Spain, which may affect the generalizability of the findings to other regions with different climatic, economic, or regulatory conditions. Additionally, while expanding the study to cover more years and neighboring buildings could

provide a broader perspective on energy consumption and optimization, data availability poses a significant challenge. Access to long-term and multi-location energy data is often restricted due to privacy concerns, measurement inconsistencies, or institutional constraints. Future research could benefit from improved data-sharing policies and collaborations to enhance the applicability of the findings across diverse locations.

Moreover, while the study evaluated several machine learning models, including Random Forest, linear models, SVR, and Neural Networks, it did not explore time-series models such as Long Short-Term Memory (LSTM) networks or ARIMA. These models, which are specifically designed to capture sequential dependencies in time-dependent data, could potentially improve performance by better modeling the temporal patterns inherent in energy consumption. Future research could explore the application of these models to address this limitation and enhance predictive accuracy.

B. Workflow

Figure 1 shown below illustrates the step-by-step process of predicting building energy consumption using regression models. It begins with data collection, where the hourly energy consumption and environmental conditions (temperature, humidity, precipitation) are gathered for a time span of a year. The next step, data preprocessing, addresses missing values and prepares the data for analysis. Feature engineering follows, creating essential temporal variables like Hour, Day of Year, and Is Weekend to capture energy usage patterns effectively. After the data is processed, various regression models are selected for comparison, including Linear Regression, Ridge and Lasso Regression, SVR, KNN, Random Forest, XGBoost, and Neural Networks. These models are then trained in the model training step using the preprocessed data. Performance is assessed to determine the best model based on evaluation metrics such as MAE and R^2. The final results interpretation and insights stage derives conclusions that help in optimizing building energy consumption.

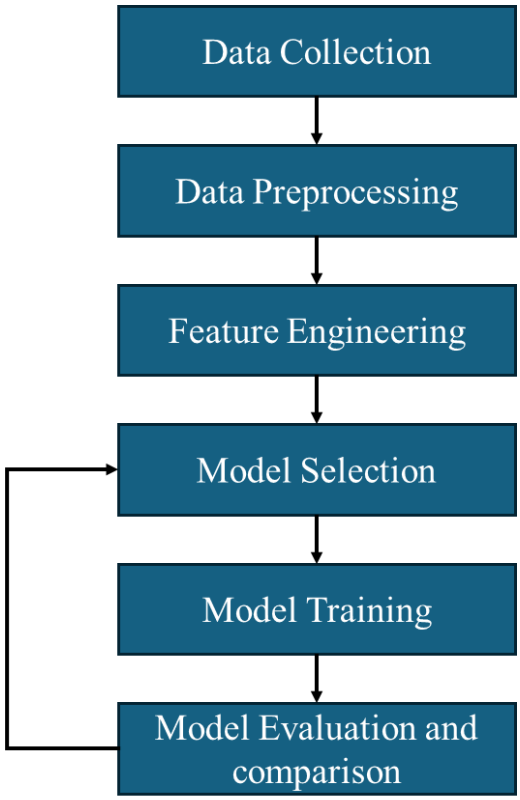

Figure 1: Flowchart for finding the best AI model.

Finally, the results are thoroughly discussed and interpreted to identify the best-performing model based on various evaluation metrics. This involves comparing model performance across different criteria, such as accuracy, precision, recall, and overall prediction reliability. After selecting the best model, feature interpretation is introduced as a crucial step to ensure the model's alignment with reality and its ability to provide meaningful insights. Feature importance techniques, such as SHAP is utilized to assess the contribution of individual features to the model's predictions. This step is critical for validating the model’s decisions and ensuring that the selected features make logical sense in the context of the problem. Additionally, feature interpretation helps in understanding whether the model is capturing the correct relationships between input variables and the target variable, ensuring consistency with domain knowledge and real-world expectations.

C. Dataset

Using hourly energy usage records for two buildings over the span of 3 years, the "Building Energy Consumption Dataset" from Mendeley Data is used in this study [18]. Key features of the dataset include the following: weather variables (minimum, maximum, and average temperature), precipitation (PRECTOT), humidity (RH2M), and energy consumption (the target variable) measured in kWh. Temporal variables include the hour, day of the week, weekend indicator, and day of the year. This dataset, which is openly accessible, provides enough variation to facilitate the creation and assessment of machine learning models.

This study investigates many regression models to forecast energy usage, each with its advantages. Multiple linear regression is a simple method for modeling linear connections. An ensemble technique called Random Forest Regression reduces overfitting and improves generalization by mixing many decision trees to increase accuracy and stability. Ridge and Lasso Regression maintains predictive strength while avoiding overfitting by introducing regularization. Support Vector Regression (SVR) uses support vector machines to deal with nonlinear connections. Using the average of the nearest data points in feature space, K-Nearest Neighbors (KNN) makes value predictions. Furthermore, Neural Networks offer a more sophisticated and adaptable method for identifying intricate patterns in energy usage data.

Additionally, the performance of each model has been assessed using Mean Absolute Error (MAE) and R-squared (R^2) metrics, standard measures for regression performance. The process details have been assessed through data preprocessing, model building, evaluation, and comparison of different machine learning techniques for predicting building energy consumption. The models' effectiveness is measured using predictive accuracy and interpretability to identify the best approach for energy consumption forecasting. The dataset used in this research study consists of hourly energy consumption data from a building, providing insights into how energy usage fluctuates across time in response to various internal and external factors. The target variable, Energy Consumption (ENERGY), represents the energy consumption in kilowatt-hours (kWh) at each hour. Several features related to environmental conditions, including temperature, humidity, and precipitation, are also provided. Specifically, the dataset includes columns like T2M, T2M_MIN, and T2M_MAX, representing

the average, minimum, and maximum temperatures recorded during each hour. These temperature features are crucial as they could impact the building's heating and cooling needs. RH2M represents the relative humidity, which can also influence energy usage, particularly concerning HVAC (heating, ventilation, and air conditioning) operations.

D. Data Preprocessing

In addition to environmental variables, the model includes temporal features such as Hour, DayOfYear, and IsWeekend to capture the effect of time on energy consumption patterns. The Hour feature provides information on the specific time of day, which is essential in understanding daily usage patterns, while DayOfYear tracks seasonal variations. IsWeekend serves as a binary indicator, reflecting whether the observation falls on a weekend, which may have a different energy consumption pattern due to reduced occupancy or different operational schedules in the building. This dataset provides a comprehensive foundation for predicting energy consumption, combining environmental, temporal, and building-specific factors.

The first step in preparing the machine learning data was handling missing values. The dataset was checked for missing or null entries, which are common in real-world data and can cause issues during model training. Any rows containing missing values were removed to ensure that only complete records were used. This decision was made based on the fact that missing data could introduce bias or reduce the quality of predictions. After removing rows with missing values, the dataset became more consistent and ready for further processing. A feature selection was conducted to identify the most relevant features for predicting energy consumption. Certain features, such as PRECTOT (total precipitation) and RH2M (relative humidity), ALLSKY (radiation) were dropped from the dataset after performing feature importance analysis as shown in Figure 2 (this is just a sample from the random forest method, but all other feature importance show similar results).

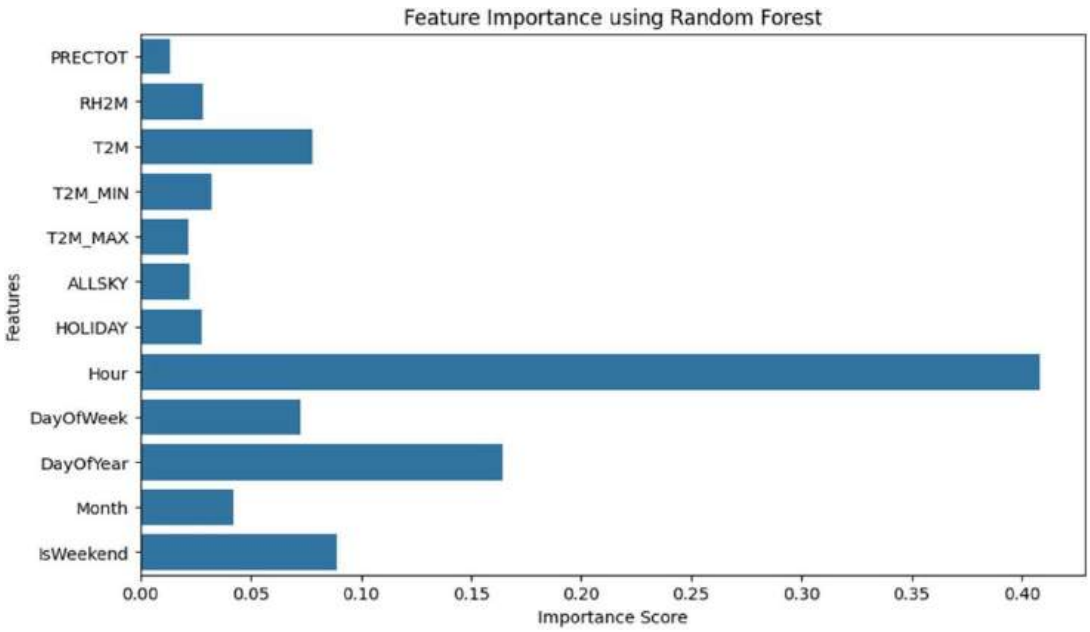

Figure 2 Feature Importance results using Random Forest

This step was crucial, as it reduced dimensionality and removed variables that did not significantly contribute to the prediction model. By eliminating unnecessary features, the model could focus on the variables with the highest predictive power, such as temperature and temporal features. Afterward, feature engineering was utilized, where the DATE column was transformed into useful time-based features. The original DATE column, which included both the date and hour, was split to extract the hour of the day, the day of the year, and a binary feature indicating whether the day was a weekend. These temporal features are important because they help capture daily, weekly, and seasonal patterns in energy consumption, which are crucial for making accurate predictions. Including a weekend indicator, for example, helps the model account for potential differences in energy consumption between weekdays and weekends, which can be influenced by factors such as occupancy and operational schedules.

To ensure that all features were comparable, standard scaling was applied for all methods except the Min-Max Scaler for the Neural Network. Scaling is particularly important for machine learning algorithms sensitive to the magnitude of input features, such as Support Vector Regression (SVR) and K-Nearest Neighbors (KNN). The Min-Max Scaler transforms the data so that all features are scaled to a range between 0 and 1, making the models less biased toward features with larger numeric ranges. This normalization process ensures that the model treats

each feature equally, preventing one feature from dominating the learning process. In addition, a train-test split has been implemented to evaluate the model's performance. The data was divided into training and testing sets, with 80% of the data used for training and the remaining 20% reserved for testing. This approach allows for proper validation and helps prevent overfitting, ensuring the model can generalize well to unseen data.

IV. RESULTS AND DISCUSSION

This study evaluates several machine learning models based on their performance in predicting energy consumption, measured by Mean Absolute Error (MAE), Mean Squared Error (MSE), and R-squared (R^2). Table 1 summarizes the performance of each method used in this project.

Table 1 Results of the various regression models.

MODEL	MEAN ABSOLUTE ERROR (MAE)	MEAN SQUARED ERROR (MSE)	R^2
LINEAR REGRESSION	50.08	4216.94	0.197
RANDOM FOREST	8.33	242.08	0.954
XGBOOST	17.14	700.26	0.867
RIDGE REGRESSION	49.31	4101.75	0.219
LASSO REGRESSION	49.97	4183.10	0.203
SVR	35.18	2882.00	0.451
KNN	18.38	910.94	0.826
NEURAL NETWORK	**18.64**	**806.03**	**0.85**

The regression model results reveal significant differences in predictive performance for energy consumption. Among the evaluated models, Random Forest emerges as the best performer, achieving the lowest Mean Absolute Error (MAE) of 8.33, a Mean Squared Error (MSE) of 242.08, and the highest R-squared (R^2) of 0.954. This indicates that the model explains approximately 95.4% of the variance in the data, as shown in Figure 3.

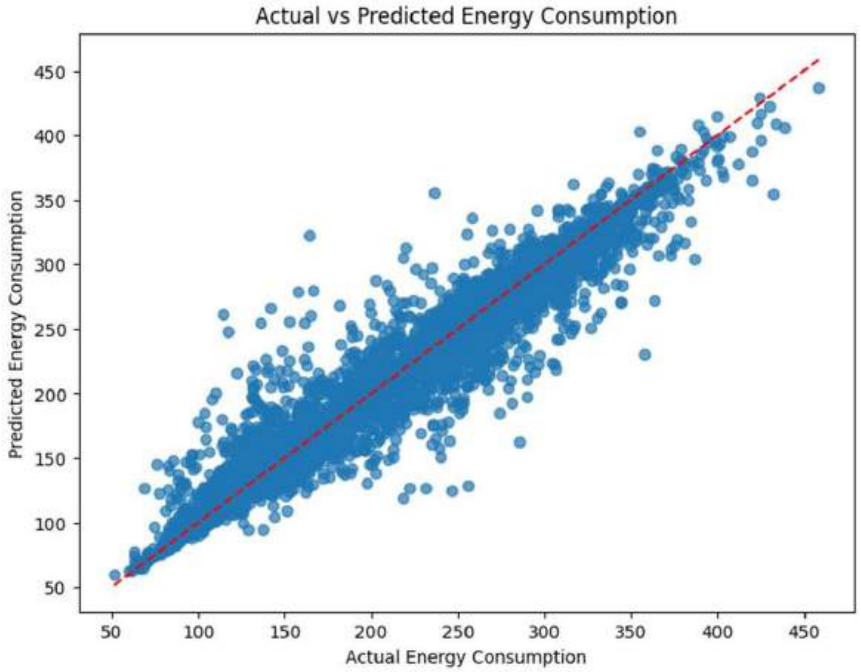

Figure 3 Predicted Energy consumption vs actual

XGBoost also demonstrated strong predictive accuracy, achieving an MAE of 17.14, MSE of 700.26, and an R^2 of 0.867, though it was slightly less effective than Random Forest. K-Nearest Neighbors (KNN) followed with an MAE of 18.38, MSE of 910.94, and an R^2 of 0.826, indicating good performance but higher error rates compared to tree-based models. In contrast, Support Vector Regression (SVR) had a significantly higher MAE of 35.18, MSE of 2882.00, and a relatively low R^2 of 0.451, suggesting it was less effective at capturing underlying patterns in the data. The Neural Network model trained smoothly without overfitting, as shown in Figure 4. It produced decent results with an MAE of 18.64, MSE of 806.03, and an R^2 of 0.85, outperforming SVR but falling behind Random Forest and XGBoost in predictive accuracy.

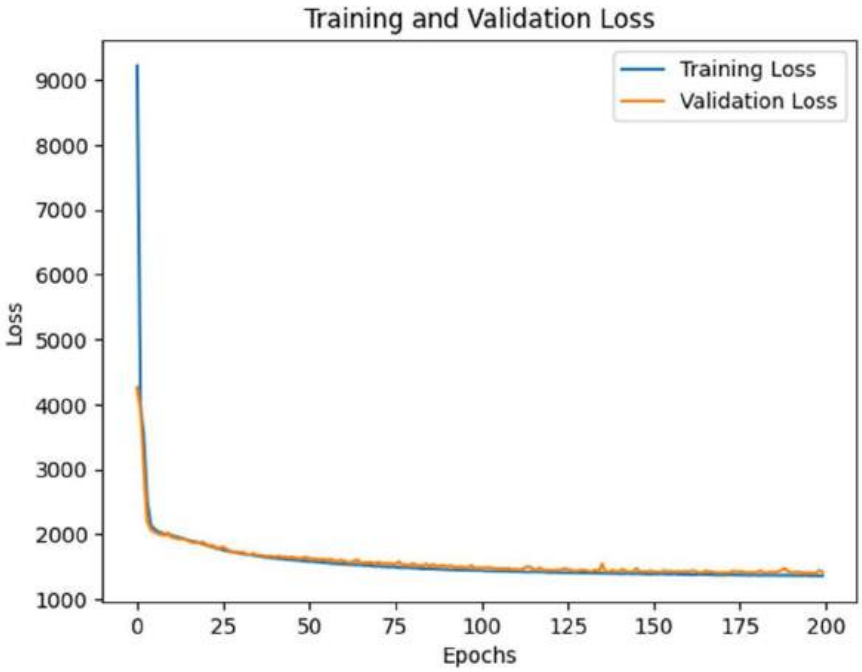

Figure 4 Training process of the neural network

However, further tuning and testing can be done on the Neural Network. As discussed previously a feed forward Neural Network consists of and input and out layer and hidden layers in between, where each layer consists of certain number of neurons. The learning algorithm used was Adaptive Moment Estimation optimizer (Adam) is an optimization algorithm that combines the advantages of momentum and adaptive learning rates. It computes individual learning rates for each parameter using estimates of the first and second moments of the gradients, enabling efficient and robust training of deep learning models. However, the learning rate can be changed and tuned. Different structures of number of layers, neurons and learning rates were tested and evaluated. The results of this tuning can be shown in Table 1.

Table 1 performance results for different Neural Networks

Layers-neurons	**LEARNING RATE**	**MEAN ABSOLUTE ERROR (MAE)**	**MEAN SQUARED ERROR (MSE)**	**R^2**
64	0.0010	27.860467	1739.491082	0.668633
128-64	0.0010	24.186951	1404.341130	0.732478
128-64-32	0.0010	21.331557	1061.582213	0.797773

64	0.0100	27.398675	1590.457467	0.697024
128-64	0.0100	19.685038	903.640517	0.827860
128-64-32	**0.0100**	**18.639559**	**806.029579**	**0.846454**
64	0.0001	35.197151	2326.152578	0.556877
128-64	0.0001	26.667670	1688.658357	0.678317
128-64-32	0.0001	25.715233	1539.650502	0.706702

It can be noted that the maximum achieved R^2 value achieved was approximately 0.84 which enhanced the original Neural Networks performance but still slightly under performing the random forest method.

Ridge and Lasso Regression exhibited poor performance, with high MAE values (49.31 and 49.97, respectively) and low R^2 scores (0.219 for Ridge and 0.203 for Lasso), likely due to their inability to capture the complexities in the data. Similarly, Linear Regression performed poorly, with an MAE of 50.08, MSE of 4216.94, and an R^2 of 0.197, suggesting that the linear assumptions do not hold for this problem. Figure 5 illustrates the performance of the Ridge regression method.

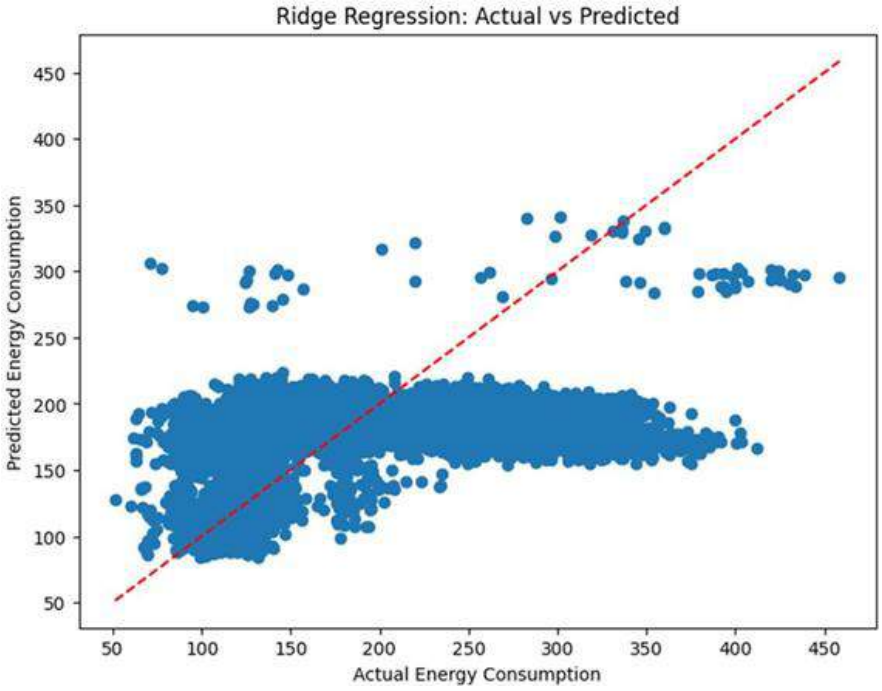

Figure 5 Ridge regression performance

The results suggest that tree-based models, particularly Random Forest, are the most suitable for this energy consumption prediction task. In contrast, linear models and Support Vector Regression (SVR) struggle to capture the data's complexities effectively. For building managers, these findings highlight the potential for implementing more advanced machine learning models, like Random Forest, to improve the accuracy of energy consumption forecasts. Furthermore, feature interpretability is done using SHapley Additive exPlanations (SHAP) [19]. SHAP is a machine learning interpretability method based on game theory, designed to explain individual predictions of machine learning models. It provides a unified approach to understanding model outputs by calculating the contribution of each feature to a particular prediction. The SHAP summary plot (Figure 6) shows how different features impact energy consumption predictions. "Hour" influences energy use significantly, with higher values in the evening leading to increased consumption, while early hours reduce it. "IsWeekend" indicates higher energy use on weekends compared to weekdays. "T2M" (temperature) has a mixed effect, with higher temperatures slightly increasing energy consumption, likely due to cooling needs. "DayOfYear" shows minimal impact on energy use, with no clear trend. Overall, the plot reveals the key factors that drive energy consumption based on time of day, weekends, temperature, and seasonal variations.

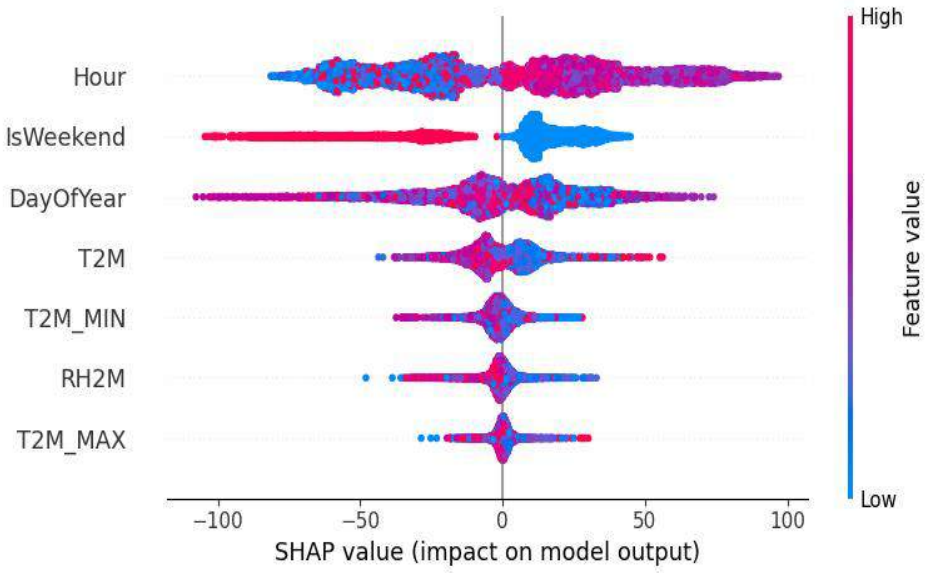

Figure 6 SHAP summary plot

Such predictions can inform better decision-making in energy optimization, leading to cost savings and more efficient resource management. Building managers can leverage these insights to implement strategies that reduce energy consumption, optimize heating and cooling schedules, and ultimately lower operational costs. Future research could explore how these models could be integrated into real-time energy management systems.

V. CONCLUSIONS

This study aimed to predict building energy consumption using various machine learning regression models. The dataset included hourly energy consumption data along with weather and temporal features. After preprocessing—handling missing values, feature selection, and scaling—several regression models were applied, including Linear Regression, Random Forest, Ridge and Lasso Regression, Support Vector Regression (SVR), K-Nearest Neighbors (KNN) and feedforward Artificial Neural Networks (ANN). Model performance was evaluated using Mean Absolute Error (MAE) and R-squared (R^2) to assess accuracy and generalization. Among the models, Random Forest Regression achieved the best performance, with an MAE of 8.33, MSE of 242.08, and an R^2 of 0.954, indicating its strong predictive power. XGBoost followed closely, with an MAE of 17.14 and an R^2 of 0.867. Ridge Regression also showed unacceptable accuracy (MAE: 49.31, R^2: 0.219), while simpler models like Linear Regression (MAE: 50.08, R^2: 0.197) struggled with the dataset's complexity. SVR performed poorly as well, with an MAE of 35.18 and an R^2 of 0.451, demonstrating its limitations in capturing energy consumption patterns. Furthermore, ANN performed really well where originally they performed slightly worse than KNN however after tuning and optimizing hyper parameters the neural network was able to outperform KNN but still slightly underperforms XGBoost and random forest. Overall, the results highlight the effectiveness of ensemble methods and regularized models in handling complex relationships, while traditional linear approaches were less effective for this task.

The findings of this study have significant implications for the field of energy consumption prediction. By comparing different machine learning models, the study highlights the importance of using ensemble methods and regularized models, which are more adept at handling complex, non-linear relationships in energy data. The strong performance of Random

Forest and XGBoost suggests that these models can be valuable tools for energy forecasting, potentially assisting building managers and policymakers in making more accurate energy usage predictions and decisions. Additionally, the study provides insights into model selection, guiding future work in energy efficiency, optimization, and demand forecasting, ultimately contributing to more sustainable energy practices and better resource management.

VI. EXTENSIVE STUDIES

Although this study achieved promising results, several avenues for improvement and further exploration exist. First, including more granular or diverse data, such as building-specific features (e.g., floor area, insulation type, occupancy schedules) and additional weather parameters (e.g., wind speed, cloud cover), could enhance model performance. Moreover, time-series forecasting techniques, such as ARIMA or LSTM (Long Short-Term Memory) networks, could be explored to better capture the temporal dynamics and sequential dependencies in energy consumption.

Additionally, feature engineering can be expanded by exploring advanced techniques such as creating interaction terms between weather and temporal features or incorporating external factors like holidays and special events. Hyperparameter optimization and cross-validation can also be further refined to improve the robustness of the models.

Acknowledgments

The US Department of Energy funds this study under DE-EE0009728.

References

1. R. Amano, M. I. Youssef and M. A. Youssef, "Exploring the Correlation Between Energy Intensity and Specific Energy Consumption in Food And Kindred Industry for the Midwest States," International Journal of Energy for a Clean Environment, Vol. 26, No. 4, 2025.

2. R. Amano, M. A. Youssef, M. I. Youssef, "Employing Linear Regression Analysis: Investigating The Relationship Between Energy Intensity and Specific Consumption in U.S. Midwest Plastic Production Facilities," International Journal of Energy for a Clean

Environment, 2025.

3. J. Dong, J. Gao, J. Yu, L. Kong, N. Jiang and Q. Wu, "Leveraging AI Algorithms for Energy Efficiency: A Smart Energy SystemPerspective," Advances in Artificial Intelligence, Big Data and Algorithms, pp. 57-64, 2023.
4. G. Uyanık and N. Güler, "A Study on Multiple Linear Regression Analysis," Procedia - Social and Behavioral Sciences, vol. 106, p. 234–240, 2013.
5. M. I. Youssef and B. Webster, "A multi-criteria decision making approach to the new product development process in industry," in Reports in Mechanical Engineering, 2022.
6. M. I. Youssef and Y. M. Hausawi, "Utilizing the enterprise architecture model to develop the structure of public sector entities in Saudi Arabia,," Journal of Engineering Management and Systems Engineering, vol. 3, no. 3, pp. 164-174, 2024.
7. S. Cutler, D. Cutler and J. Stevens, "Random Forests," in Ensemble Machine Learning: Methods and Applications, Springer, 2011, pp. 157-176.S.
8. D. Kobak, J. Lomond and B. Sanchez, "The optimal ridge penalty for real dimensional data can be zero or negative due to the implicit ridge regularization," The Journal of Machine Learning Research, vol. 21, no. 1, pp. 6863-6878, 2020.
9. S. K. Safi, M. Alsheryani, M. Alrashdi, R. Suleiman and D. Awwad, "Optimizing Linear Regression Models with Lasso and Ridge Regression: A Study on UAE Financial Behavior during COVID-19," Migration Letters, vol. 20, no. 6, pp. 139-153, 2023.
10. K. Pelckmans, I. Goethals, J. D. Brabanter and B. De Moor, "Componentwise Least Squares Support Vector Machines," in Support Vector Machines: Theory and Applications, 2005.
11. D. Basak, S. Pal and D. Chandr, "Support Vector Regression," Statistics and Computing, vol. 11, no. 10, 2007.
12. Z. Zhang, "Introduction to machine learning: K-nearest neighbors," Annals of Translational Medicine, vol. 4, no. 11, pp. 218-218, 2016.

13. Z. Zhang, "Too much covariates in a multivariable modelmay cause the problem of overfitting," Journal of Thoracic Disease, vol. 6, no. 9, pp. E196-E197, 2014.

14. O. Farghaly and P. Deshpande, "Fully convolutional neural network-based segmentation of brain metastases: a comprehensive approach for accurate detection and localization," vol. 36, p. 20711–20722, 2024.

15. M. Islam, G. Chen and S. Jin, "An Overview of Neural Network," American Journal of Neural Networks and Applications, vol. 5, no. 1, p. 5, 2019.

16. O. Farghaly and P. Deshpande, "Leveraging Machine Learning to Predict National Basketball Association Player Injuries," 2024 IEEE International Workshop on Sport, Technology and Research (STAR), pp. 216-221, 2024.

17. A. K. Sleiti, S. Gowid, . W. A. Al-Ammari and Y. AbuShanab, "Accurate prediction of dynamic viscosity of polyalpha-olefin boron nitride nanofluids using machine learning," Heliyon, vol. 9, no. el6716, 2023.

18. Mariano, Deyslen (2024), “Building Energy Consumption Datasets”, Mendeley Data, V1, doi: 10.17632/mzkyh37mtr.1

19. J. Zhang, X. Ma, J. Zhang, D. Sun, X. Zhou, C. Mi, H. Wen, "Insights into geospatial heterogeneity of landslide susceptibility based on the SHAP-XGBoost model," Journal of Environmental Management, vol. 332, p. art. no 117357, 2023.

Author Biographies

Yazeed AbuShanab is a mechanical engineering graduate with a master's degree and a PhD candidate at UWM. Currently an energy engineer at UWM-ITAC, their research focuses on energy systems, pipeline leakage detection, and thermodynamic property approximation using AI, integrating engineering and AI for innovative energy solutions.

Mohamed I. Youssef, a Ph.D. candidate and research assistant at UWM, holds an MSc from Florida Tech and a BSc in Mechanical Power Engineering. With experience in academia and industry, he specializes in project management, energy systems, wind turbines, and renewable energy. He holds CEM®, PMP®, RMP®, C-KPIP®, and CMRP® certifications.

Omar Shaker is a PhD candidate in Mechanical Engineering at the University of Wisconsin-Milwaukee, working under Professor Ryo Amano. As the Team Lead at UWM's Industrial Training and Assessment Center (ITAC), his research focuses on dual-rotor wind turbine performance, airfoil optimization, and energy efficiency. He contributes significantly to publications and training initiatives.

Mohamed Abdelaziz Youssef, M.E., is a Ph.D. candidate in Mechanical Engineering at the University of Wisconsin-Milwaukee and serves as an Energy Auditor at the Industrial Training and Assessment Center. He brings over seven years of professional experience in industrial process analysis, with a focus on enhancing energy efficiency and optimizing system performance.

Prof. Ryo Amano is the Richard & Joanne Grigg Fellow Professor, and Alan D. Kulwicki Fellow Professor, specializes in fluid mechanics, heat transfer, and energy systems. His research covers gas turbines, rocket engines, propulsion, aerodynamics, wind and hydro energy, biomass combustion, and wastewater treatment. He leads funded projects from NSF, DOE, NASA, and others and directs the DOE-funded Industrial Assessment Center.

International Journal of Energy Efficiency Engineering (IJEEE)
Volume 1, Issue 1 (May 2025), pages 27-47

INTERNATIONAL JOURNAL OF
ENERGY EFFICIENCY ENGINEERING

The Effect of SiO_2 Nanoparticle on the Mechanical Properties of Silica-Epoxy Nanocomposites-An Experimental Study

Ryan Masoodi[1], Parinaz Heydar, and Md Saiful Islam

School of Design and Engineering, Thomas Jefferson University, 4201 Henry Ave, Philadelphia, PA 19144, USA

Abstract

Polymer nanocomposites, featuring reinforcing particles smaller than 100 nm, exhibit superior mechanical properties compared to conventional composites. This study investigates the effect of nanoparticle size and weight fraction on the Young's modulus and tensile strength of epoxy-silica nanocomposites. To evaluate their mechanical behavior, epoxy-silica samples were prepared using nanoparticles sized 15 nm, 20 nm, and 80 nm at 3% and 5% weight fractions. Ultimate stress, yield stress (0.2%), maximum strain, and Young's modulus were measured. Results showed that adding silica nanoparticles enhanced the ultimate tensile stress, yield stress, and Young's modulus of pure epoxy. Notably, nanocomposites with 80 nm particles at 3% loading displayed the highest strain. At 5% loading, 20 nm nanoparticles exhibited the highest tensile strength and stiffness among the tested samples, while 15 nm particles showed comparatively lower improvements, likely due to increased agglomeration. Additionally, a general trend of increased stiffness was observed with smaller particle sizes, although deviations occurred due to dispersion and porosity effects.

[1] Corresponding author: Dr. Ryan Masoodi, Tel: +1-215-951-5630, Email: ryan.masoodi@jefferson.edu

Keywords: *Polymer Nanocomposites; Nanoparticle; Tensile stress; Young's modulus; Silica-epoxy.*

I. INTRODUCTION

A. Nanocomposites

Nanocomposites are advanced materials that integrate nanoscale reinforcements into a matrix material (polymer, metal, or ceramics) to achieve synergistic mechanical, thermal, electrical, and optical properties superior to conventional composites. These multi-phase nanomaterials have at least one dimension in the nanometer scale (10^{-9}m). The nanoparticles are often in the form of nanofibers, nanotubes, nanoclays, or spherical nanoparticles. A prominent area of research in nanotechnology is polymer nanocomposites (PNCs). The major advantage of PNCs is improved mechanical properties with small filler loading levels. An important thermosetting polymer used in nanocomposites is epoxy resin. It was selected for this research due to its broad applicability and combination of mechanical strength, chemical durability, adhesion, and thermal performance. Epoxy nanocomposites are multifunctional materials with the potential for lower-cost, high-performance applications in adhesives, coatings, electronics, automotive, aerospace, and marine industries, where lightweight structural components with optimal mechanical properties are preferred [1] [2] [3] [4].

B. Effects of Filler Size and Loading

Generally, the large surface-area-to-volume ratio of nanoparticles increases the available interfacial contact within nanocomposites, enabling effective load transfer between the filler and polymer matrix and ultimately enhancing the mechanical strength [3]. Particle–particle interactions also significantly influence nanocomposite mechanical performance. Unlike particle-matrix interaction, which improves mechanical strength, particle-particle interaction has an undesirable effect. Interparticle attraction and repulsion, governed by van der Waals and electrostatic forces, can lead to agglomeration or clustering of nanoparticles. The dense and strong particle collectives are called aggregation, whereas agglomeration refers to looser, larger structures that their mechanical forces can easily break. High loadings of large nanoparticles produce aggregation and weak interfacial properties, negatively impacting tensile strength [5]. Interparticle forces can be tuned through variations in particle size, concentration (wt.% or vol.%), and surface

treatments. Research optimizing nanocomposite performance has focused on tailoring particle dimensions and filler content, including size, weight, and volume fractions, in recent years [5] [6] [7] [8] [9] [10].

Fu et al. comprehensively examined how particle dimensions, loading levels, and filler–matrix bonding influence nanocomposite mechanical behavior [11]. They concluded that each of the three factors plays an important role in nanocomposites' strength and toughness properties; higher particle loadings were found to improve stiffness significantly, and for a given volume fraction, the strength increased with decreasing particle size [11]. Increasing nanoparticles' weight fraction has been reported to improve Young's modulus in nanocomposites significantly. Singh et al. reported a maximum increase in elastic modulus with 4 wt.% SiO_2 nanoparticles dispersion in an epoxy matrix [12]. Filippov et al. reported a 25% increase in the modulus of elasticity when the content of silicon dioxide nanoparticles in the epoxy resin was increased to 5 wt.% [13]. Soni et al. showed that adding 0.5 wt.% of SiO_2 nanoparticles, improved the elastic modulus, ultimate tensile strength, and failure strain of the SiO_2 epoxy nanocomposites by 18%, 15%, and 33%, respectively [14]. Studies have also shown that the interfacial bonding strength and thickness determine the mechanical properties of nanocomposites [15]. The surface modification of silica nanoparticles positively impacts the interfacial region of epoxy nanocomposites. Battistella et al. found that in silica-epoxy nanocomposites, the fracture toughness significantly increased by 54% by adding only 0.5 vol% of surface-modified fumed silica [16]. Islam et al. developed empirical models to predict the mechanical performance of silica–epoxy composites across different particle sizes and loadings, as shown in Table 1 [17].

In Table 1, E is Young's modulus, σ is tensile stress, SSA is specific surface area in m^2/kg, g is gravitational acceleration in m/s^2, A is the average surface area of nanoparticle in m^2, W is the average weight of nanoparticles in N, wt., and vol are weight and volume fractions [$0 \leq \text{wt} \leq 100, 0 \leq \text{vol} \leq 100$], σ_{cy} is the compressive yield stress, and E_c is the compressive modulus, [17].

Table 1: Suggested expressions to estimate the mechanical behavior of silica-epoxy nanocomposites at different weight fractions of nanoparticles [17].

Nanocomposite	**Suggested equation**	**Ranges of applications**		
		Nanoparticle dimension	**wt.% or vol.%**	**Remark**
Silica-epoxy	$E = 3.639 \times 10^4 \frac{W}{A} wt^{0.04}$ [in GPa]	8-50nm	1-40 (wt.%)	Sol-gel processing
Rubbery silica epoxy mesocomposite	$E = \frac{g}{SSA} 288 \times 10^{0.053wt}$ [in GPa]	10-100nm	2-10 (Wt.%)	Nanoparticle's pore size: 4-21 nm
Silica-epoxy	$\sigma = \frac{w}{A} 10^6 \times wt^{-0.069}$ [in MPa]	8-50nm	1-40 (wt.%)	Sol-gel processing
Rubbery silica epoxy mesocomposite	$\sigma = \frac{g}{SSA} 55.8 \times 10^{0.04wt}$ [in GPa]	10-100nm	2-10 (wt. %)	Nanoparticle's pore size: 4-21 nm
Epoxy-silica-rubber	$\sigma_{cy} = 56.8 \times 10^{-0.004vol}$ [in MPa]	20nm, 80nm	0-6.4 (vol.%)	CTBN processing
Epoxy-silica-rubber	$E_c = 1.53 \times 10^{0.001vol}$ [in GPa]	20nm, 80nm	0-6.4 (vol.%)	CTBN processing

C. Health Concerns and Safety Issues

Nanotechnology has significant environmental, health, and safety (EHS) concerns, particularly in product application and safe utilization of nanoparticles. Nanoparticles can be combustible and initiate catalytic reactions, so precautions should be taken to reduce exposure during processing, maintenance, machining, sanding, and drilling processes. Toxicological responses are influenced by particle size, geometry, surface area, and surface reactivity. Prediction of health risks depends on routes of exposure, translocation, toxicity, duration, and immune system effects. Control of

airborne exposure can be achieved using personal protective equipment and risk management programs. Sub-100 nm diameter nanotechnologies have been found to affect the human heart and lung, and agglomerates of 20nm titania (TiO_2) nanoparticles and pigment grade TiO_2 have a great impact on animal lungs due to their nanoscale nature [18]. All nanoparticle handling was conducted in a designated area with controlled ventilation to minimize exposure risks. Researchers wore appropriate personal protective equipment, including N95 respirators, nitrile gloves, lab coats, and safety goggles. Nanoparticle containers were only opened within a ventilated enclosure to prevent aerosolization. All waste materials containing nanoparticles were collected in sealed containers and disposed of according to institutional hazardous waste protocols.

Most previous studies have examined the effects of particle weight fraction, volume fraction, or surface modification on the mechanical behavior of nanocomposites. Consequently, the interaction between particle size and weight fraction on mechanical performance remains insufficiently explored, particularly under controlled experimental conditions. Understanding the synergistic and individual effects of particle size and weight fraction is essential. This requires controlling all other parameters while varying only one variable, such as maintaining a constant weight fraction while altering particle size. Such an approach helps isolate the effects of particle size from other variables and supports the interpretation of trends in strength and stiffness. Additionally, it helps identify trends in mechanical behavior associated with different nanoparticle sizes and loading levels while acknowledging the limitations of the selected size resolution. This study utilized silica nanoparticles of different sizes (15 nm, 20 nm, and 80 nm) as nano-fillers. The weight fraction was kept constant at 3% and 5% to isolate the effect of particle size. The mechanical properties of the prepared nanocomposites were measured and compared to those of pure epoxy specimens.

The key contributions and novelty of this study are:

- Introduces an experimental design to assess the combined effect of nanoparticle size (15, 20, 80 nm) and weight fraction (3%, 5%) on tensile properties of silica-epoxy nanocomposites.
- Performs indirect porosity analysis and SEM imaging to explain variations in mechanical behavior beyond raw data.
- Uses practical loading levels and commercially available silica nanoparticle sizes, reflecting real-world constraints in manufacturing and design.

- Acknowledges the limited resolution in particle sizing and proposes this as a future research direction to refine the identification of optimal nanoparticle dimensions.

II. EXPERIMENTS

A. Materials and Preparation

Fibre Glast Developments Corporation supplied 2000 epoxy resin and 2120 hardener (with a 3 to 1 mixing ratio). The silica (Silicon Oxide) nanoparticle, supplied by Nanostructured and Amorphous Materials Inc., was used as nanofillers. Silica (SiO_2) nanoparticles of three different sizes (particle diameters of 15, 20, and 80 nm) were selected for this research. All silica nanoparticles are spherical and white in color. All composite samples were made with a 5% and 3% nanoparticle weight fraction.

1. Making Samples

To make the pure epoxy samples, a water bath indirectly heated the resin to decrease its viscosity using the same condition used for composites. Then, the curing agent was added and stirred rapidly for 5 minutes using a magnetic stirrer and a hand. The mixture was poured into the mold and kept at room temperature for one day to cure.

The silica-epoxy nanocomposites were made by mixing epoxy resin with silica nanoparticles. The epoxy resin of volume 90ml (101.26 g) was poured into a small beaker while the beaker was placed inside a larger beaker filled with water. The large beaker was placed over a hot plate with a magnetic stirrer at 90°C and 1150 rpm for 30 minutes to decrease the resin's viscosity and release the bubbles. An amount of 6.96 g of silica nanoparticles (5% weight fraction of the total weight of the epoxy-hardener-silica mixture) was placed into a small beaker on a hot plate at 110°C for 30 minutes to evaporate the moisture from the particle surfaces, as silica is hydrophilic. Then, epoxy resin and silica were mixed, placed over a magnetic stirrer at 1150 rpm, and stirred rapidly for 5 minutes. Afterward, 30ml (30.9 g) of hardener was added to the mixture and then stirred using both-magnetic stirrer and hand for 5 minutes. After spraying a mold release agent, the mixture was poured into an open aluminum mold of size $162mm \times 135mm \times 4mm$.

The mold was placed on a hot plate for 60 minutes at 60°C and 1150 rpm using a magnetic stirrer and 30 minutes at 40°C. After heating and stirring, the mold was kept at room temperature for 5 hours to cure partially. The composite, partially cured at this stage, allowed a little bending, making

it easier to retrieve from the mold. The retrieved composite was maintained at room temperature for another 6 hours to cure completely.

Table 2 lists four samples with their material codes, nanoparticle weight fractions, and particle diameters. In the material code, 'E' denotes pure epoxy resin, and 'S' denotes silica nanoparticle; the next two digits after 'S' represent the diameter of the nanoparticle (in nm), and the third number after 'S' denotes the weight percentage (%) of nanoparticles in the matrix. For example, ES155 means epoxy-silica nanocomposites with a 5% nanoparticle size of 15nm.

Table 2: Material codes, particle sizes (nm), and weight fractions of nanoparticles in each nanocomposite sample.

Material code	**Particle diameter (nm)**	**Nanoparticle weight fraction (%)**
E	-	-
ES155	15	5
ES205	20	5
ES805	80	5
ES153	15	3
ES203	20	3
ES803	80	3

2. Cutting and specimen preparation

The load test specimens (also known as test coupons or dog bones) were prepared by cutting the composite sheets to the standard size using a cutting machine (Microlux band saw) having a band saw with a diamond-tipped blade. The standard ASTM D638 [19], was used to size the samples and test the tensile properties.

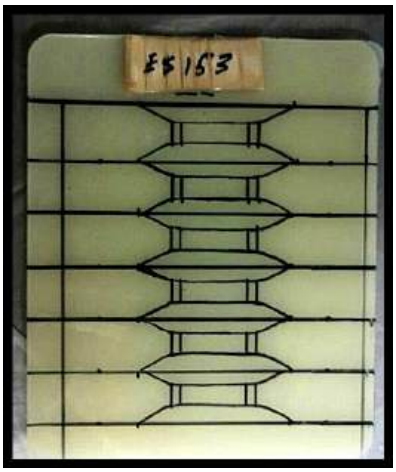

Figure 1: Prepared epoxy-silica nanocomposite (ES153) dog-bone specimens prior to tensile testing, conforming to ASTM D638 standard dimensions.

B. Mechanical Behavior

The pure epoxy and the silica-epoxy composites were tested for their mechanical (tensile) behavior according to ASTM D638 [19], Figure 2. Five specimens of pure epoxy and each composite type were prepared, considering the dimensions required by the standard. The specimens were conditioned for one hour at a temperature of 20±1ºC and a relative humidity of 65±2% before testing. The tests were performed using an Instron 5500R tensile testing machine. The crosshead speed of 1mm/min was chosen for tests, and all experiments were performed at 20±1ºC and 65±2% relative humidity. Measurements were ultimate tensile stress, maximum strain, Young's modulus, and yield stress (0.2% offset). The broken samples were used for porosity analysis (indirect porosity measurements). Some broken parts were also used to observe particle agglomerations using an SEM of the Topcon model ABT-32.

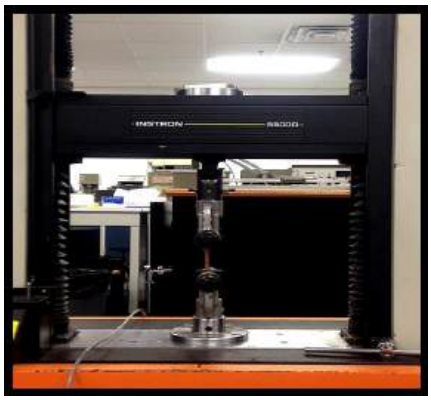

Figure 2: An experimental setup for tensile testing using the Instron 5500R machine was conducted in accordance with ASTM D638 procedures.

C. Estimation of Porosity

A factor that can significantly affect the performance of nanocomposites is the existence of voids or bubbles. The voids act as a defect to the composites, causing the composites to yield unexpected results. As a result, the theoretical density of porous composites is greater than the actual density. A decrease of two to ten percent in the mechanical properties has been reported with every one percent increase in the void content or porosity [20].

For porous composites, the volume fraction of voids or porosity ($\mathcal{E}$) is defined as:

$$\mathcal{E} = V_o/V_c \tag{1}$$

where, V_c is the volume of the composite, and V_o is the volume of the voids [20]. The total volume of the composite can be written as:

$$V_c = V_f + V_m + V_o \tag{2}$$

where, V_f is volume of the fillers (i.e., silica nanoparticles), and V_m is the volume of the matrix (epoxy resin and curing agent) [20]. The experimental density of a composite (ρ_{ce}) is defined as:

$$\rho_{ce} = \frac{m_c}{V_c} \tag{3}$$

where, m_c is the mass of composite [20]. The theoretical density (ρ_{ct}) [20], of a composite can be written as:

$$\rho_{ct} = \frac{m_c}{V_f + V_m} \tag{4}$$

Upon replacing V_o from Eq. (2) into Eq. (1) and considering Eqs. (3) and (4), the following expression is derived for the porosity:

$$\varepsilon = 1 - \frac{\rho_{ce}}{\rho_{ct}} \tag{5}$$

However, the theoretical density is related to densities of filler and matrix through the following expression [20],:

$$\rho_{ct} = \rho_f v_f + \rho_m (1 - v_f) \tag{6}$$

where, ρ_f is the density of filler, ρ_m is the density of the matrix, and v_f is the volume fraction of the filler in the composite, which can be found using the following equation:

$$v_f = \frac{\frac{m_f}{\rho_f}}{\left(\frac{m_f}{\rho_f} + \frac{m_c - m_f}{\rho_m}\right)} \tag{7}$$

where m_f is the mass of filler in the composite [20]. To find the actual or experimental density, the following equation was used:

$$\rho_{ce} = \frac{\rho_w m_c}{(m_c - m_{cw})} \tag{8}$$

where, m_{cw} is the mass of composite inside water and ρ_w is density of water [20].

D. Particle Dispersion

The degree of particle dispersion in a polymer nanocomposite is an important factor affecting the composite's performance. Uniformly distributed nanoparticles are necessary to get an efficiently reinforced polymer nanocomposite. The Scanning Electron Microscope (SEM) can be used to study particle distribution and aggregation in a nanocomposite. SEM images in both higher and lower resolution can be used to analyze the microstructure of the composite: low resolution for studying clusters and high resolution for studying agglomeration or particle dispersion. The specimens were dipped into liquid nitrogen and torn apart to observe surface morphology. A gold sputter coating with a pressure of 0.15 Torr and voltage of 1.4 kV was maintained for five minutes to prepare samples for observation.

III. RESULTS AND DISCUSSION

A. Porosity

The theoretical densities of the nanocomposite samples were estimated using the actual densities of all the six types of nanocomposites. Using Eq. (5), the indirectly measured porosities were found to be 3.39%, 1.68%, and 1.495% for nanocomposites with 15nm, 20nm, and 80nm nanoparticles, respectively, while using a 5% weight fraction of nanoparticles. The porosities were 1.7%, 1.36%, and 1.16% for nanocomposites with 15nm, 20nm, and 80nm nanoparticles, respectively, when the nanoparticle weight fraction was 3%. Table 3 shows the indirectly measured porosities of different epoxy-silica nanocomposites with 95% confidence intervals. Figure 3 shows that porosity decreases as nanoparticle size increases. It was also observed that nanocomposites with higher particle loading (wt. %) show higher porosity. These experiments generally showed an average porosity of 1.3% and 3.3% for silica-epoxy nanocomposites.

Table 3: Indirect measured mean porosities of epoxy-silica nanocomposites with 95% confidence intervals

Material code	**Porosity (%)**
ES155	3.37 ± 0.308
ES205	1.68 ± 0.135
ES805	1.49 ± 0.189
ES153	1.71 ± 0.256
ES203	1.36 ± 0.111
ES803	1.16 ± 0.16

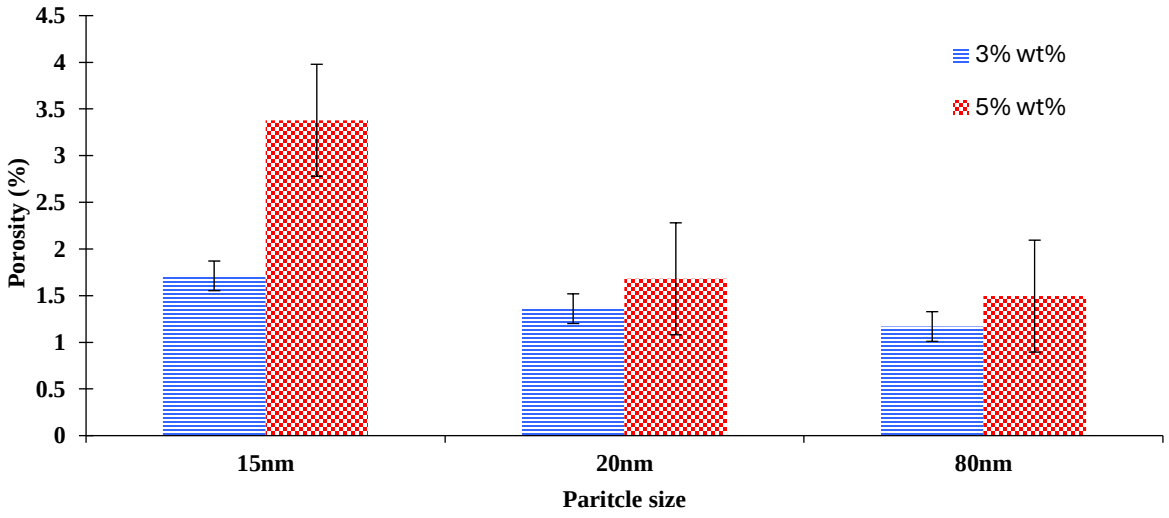

Figure 3: Indirect mean porosity measurement results with 95% confidence intervals

B. Micrographs of Nanocomposite

Particle distribution and aggregation in the nanocomposite were evaluated using an SEM analysis of fractured surfaces. Figures 4 and 5 show SEM images of different epoxy-silica nanocomposites. SEM micrographs show small clusters of nanoparticles covered by a thin polymer shell (interphase layer). Compared to the actual diameter of nanoparticles, the large particle diameter in these micrographs supports the cluster structure's formation.

All the SEM images showed a moderate degree of particle cluster dispersion with few white spots, which are nanoparticle clusters. Composite samples with 5% loading of 20 nm particles showed more pronounced clustering than the 15 nm samples, possibly due to differences in dispersion energy and particle surface behavior. Figure 4 shows low-resolution SEM images of epoxy-silica composites with 5% loadings of 15nm, 20nm, and 80nm nanoparticles with a magnification level of ×10,000. Composite samples with 5% loading of 20nm nanoparticles showed particle clusters bigger than those observed in the 15nm nanocomposite samples. Composite samples with 5% loading of 80nm nanoparticles show few river markings (related to the initiation of matrix cracks that coalescence into larger cracks, indicating the direction of propagation) and some areas with a moderate degree of particle cluster dispersion. There are also some areas with low percentages of nanoparticles, which can lead to unpredictable results in tensile behavior.

Figures 5 show SEM images of nanocomposites with a 3% weight fraction of silica nanoparticles. Figure 5a shows the composite sample with 20nm nanoparticles. There is a moderate degree of particle dispersion with few particle clusters and some smooth areas surrounded by river markings. Figure 5b shows the composite sample with 80nm nanoparticles. The river markings and smooth areas in the case of both composite samples with 3% weight fraction silica nanoparticles indicate areas of polymer matrix with a lower percentage of nanoparticles than its surrounding areas. The SEM images of composite samples with 3% loading show more river markings and smooth areas than those with 5% loading.

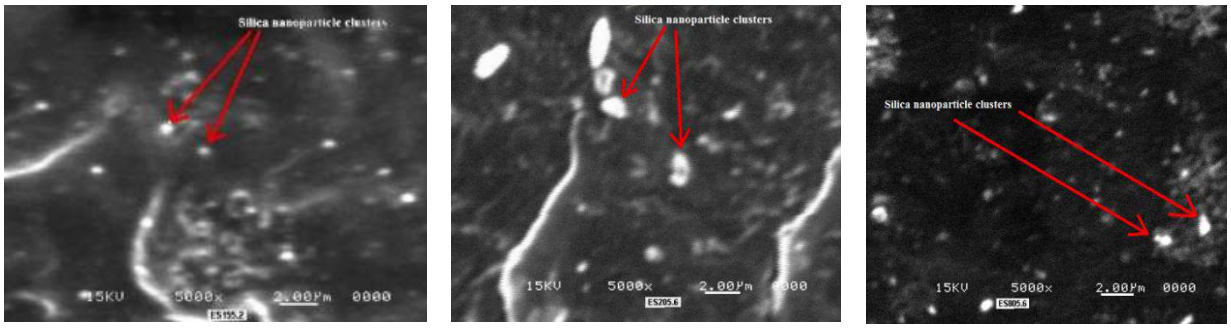

(a) (b) (c)

Figure 4: SEM images with a magnification level of ×10,000 of the surface of epoxy-silica nanocomposite filled with various silica nanoparticle diameters using 5% loading: (a) 15 nm, (b) 20 nm, and (c) 80 nm. Arrows indicate the formation of small clusters of silica nanoparticles.

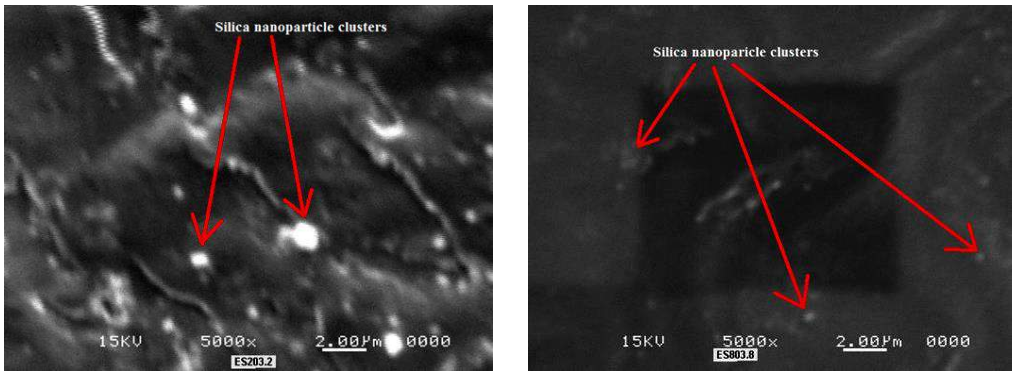

(a) (b)

Figure 5: SEM images with a magnification level of ×10,000 of the surface of epoxy-silica nanocomposite filled with various silica nanoparticle diameters using 3% loading: (a) 20 nm and (b) 80 nm. Arrows indicate the formation of small clusters of silica nanoparticles.

C. Tensile Tests

Pure epoxy and epoxy/silica nanocomposites were tested. The mean values of ultimate tensile stress, yield stress (0.2% offset), maximum strain, Young's modulus, and 95% confidence levels are illustrated in Figures 6 to 9. It can be concluded that ultimate strength, yield stress (0.2% offset), and Young's modulus of pure epoxy have improved after adding silica nanoparticles. Whenever a load is applied to the nanocomposite, it is transferred through the matrix to the nanoparticles, which have higher strength than the epoxy. Therefore, the addition of nano-silica increases the strength of the nanocomposite. The mean values of tensile properties and their 95% confidence intervals are summarized in Table 4.

The nanocomposite's gradual improvement in stiffness (Young's modulus) and strength (both ultimate tensile stress and yield stress) as the silica nanoparticle's size decreases is clearly distinguishable. A similar trend is also found when particle loading increases from 3% to 5%. (Figures 4 and 5). These mechanical property improvements can be attributed to enhanced interfacial adhesion and effective stress transfer between the silica nanoparticles and the epoxy matrix. In particular, the 20 nm particles provide sufficient interaction with the matrix without severe agglomeration in smaller 15 nm particles. Conversely, excessive porosity and clustering in the 15 nm and high-loading samples likely reduced their reinforcement efficiency, explaining the lower-than-expected tensile strength in some configurations.

Figures 6 and 7 show the ultimate tensile stress and Young's modules of nanocomposite. The Young's modulus of the nanocomposite sample with 80 nm nanoparticles with a 3% weight fraction was less than pure epoxy. Also, the pure epoxy sample had the highest ultimate strain. This unexpected result can be explained by the SEM images of a nanocomposite sample with 3% loading using an 80nm particle that showed a higher degree of unreinforced smooth areas and clusters. The reduction in strain with smaller particle sizes and higher loadings can be attributed to increased matrix rigidity and reduced ductility due to particle reinforcement. Nanoparticles restrict polymer chain mobility, reducing the material's deformability. However, the 80 nm particles at 3% loading may have acted more like micro-fillers, causing less interference with the polymer network and retaining more ductility. This explains the higher strain observed in these samples compared to smaller, more tightly interacting particles. (see Figure 3b). Overall, the mechanical behavior of

the nanocomposites is primarily influenced by nanoparticle size, dispersion quality, and porosity, as evidenced by SEM and tensile results.

Table 4: Tensile properties of pure epoxy and epoxy-silica nanocomposite (Data are mean value ± 95% confidence level).

Material code	Ultimate tensile stress (MPa)	Yield Stress (0.2% offset) (MPa)	Ultimate Strain (%)	Young's modulus (GPa)
E	34.236 ±3.53	13.138 ±0.83	2.3 ±0.31	1.38 ±0.05
ES155	41.19 ±1.96	23.896 ±2	2.30 ±0.24	1.55± 0.03
ES205	38.99 ±3.54	22.68 ±2.11	2.55 ±0.38	1.52 ±0.127
ES805	34.76 ±4.89	22.49 ±0.71	2.74 ±0.38	1.46 ±0.07
ES153	37.26 ±4.3	21.27 ±0.95	3.21± 0.49	1.46 ±0.075
ES203	35.66 ±2.49	20.92 ±0.72	3.39 ±0.24	1.45 ±0.046
ES803	34.19 ±2.67	19.498 ±1.13	3.47 ±0.33	1.34 ±0.06

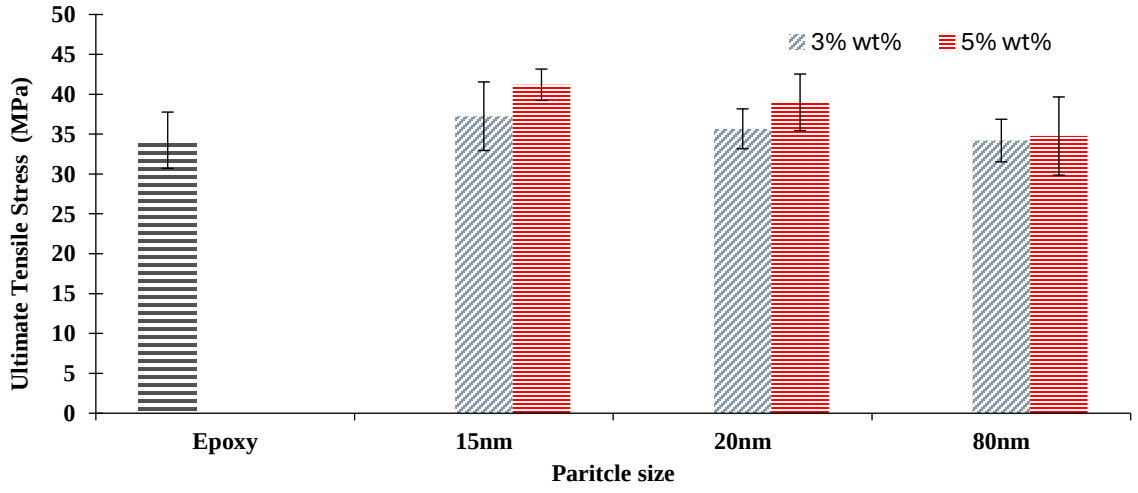

Figure 6: Ultimate tensile stress of pure epoxy and epoxy-silica nanocomposites.

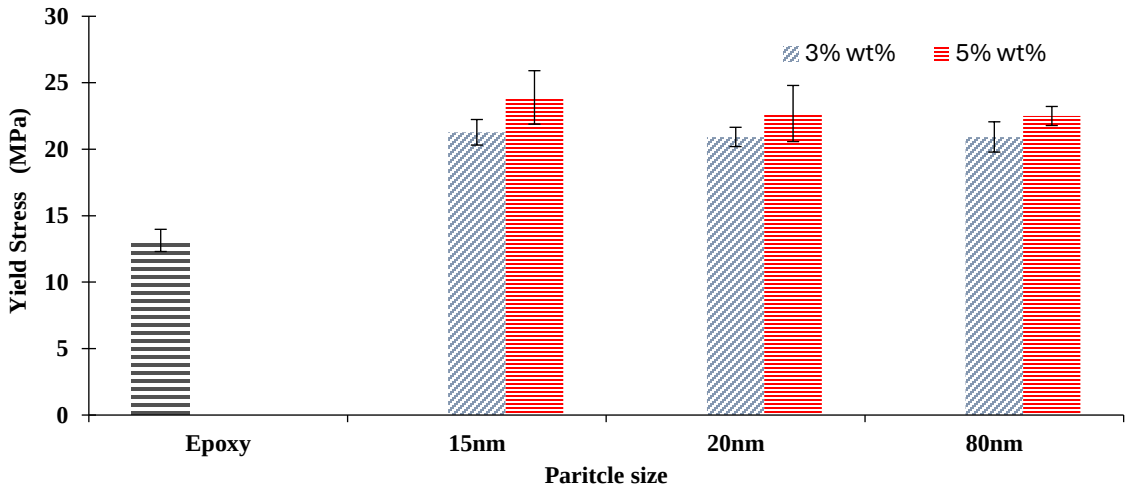

Figure 7: Yield stress of pure epoxy and epoxy-silica nanocomposites.

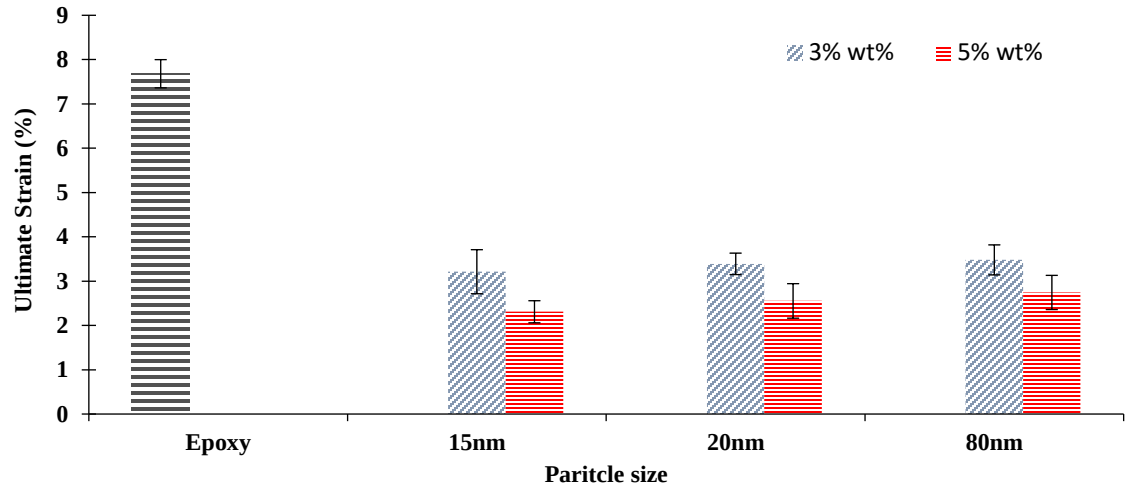

Figure 8: Ultimate Strain of pure epoxy and epoxy-silica nanocomposites.

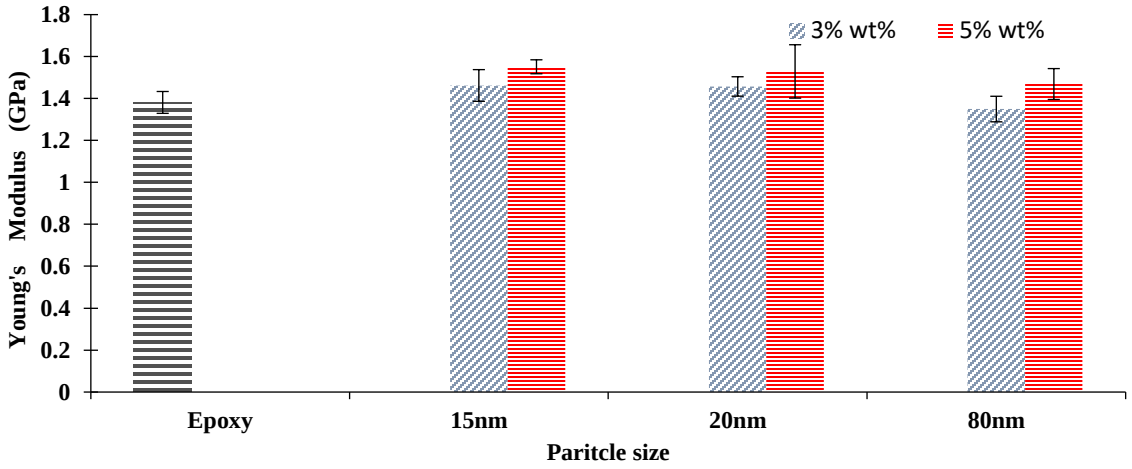

Figure 9: Young's modulus of pure epoxy and epoxy-silica nanocomposites.

IV. SUMMARY AND CONCLUSION

Pure epoxy and epoxy-silica nanocomposite specimens were prepared to investigate the impact of nanoparticle size and weight fraction on mechanical behavior. The nanocomposites contained 3% and 5% weight fractions of silica nanoparticles with diameters of 15 nm, 20 nm, and 80 nm. Specimens for tensile tests were produced following ASTM D638 standards. The mean porosity in each nanocomposite was indirectly estimated to assess the influence of porosity on mechanical properties. SEM imaging confirmed efficient nanoparticle distribution with no significant clustering. Mechanical testing revealed that adding 5% silica nanoparticles significantly enhanced the stiffness of the epoxy polymer. Among the tested sizes, the 20 nm nanoparticles yielded the highest ultimate tensile stress, yield stress (0.2% offset), and maximum strain. Additionally, the results indicated that larger nanoparticles increased the stiffness of the nanocomposite, while Young's modulus improved as particle size decreased.

Acknowledgments

The authors gratefully acknowledge the financial support provided by Thomas Jefferson University through a research grant. We thank Professor Muthu Govindaraj for fabricating the aluminum mold, Dr. Brian George and Gwenn Allen for their technical assistance with specimen preparation, and Nancy Sorkin for editing the manuscript.

References

[1] Mai, Yiu-Wing and Yu, Zhong-Zhen, *Polymer nanocomposites*. Woodhead Publishing, 2006.

[2] K. I. Winey and R. A. Vaia, "Polymer Nanocomposites," *MRS Bull.*, vol. 32, no. 4, pp. 314–322, 2007, doi: 10.1557/mrs2007.229.

[3] P. K. Balguri, D. G. H. Samuel, and U. Thumu, "A review on mechanical properties of epoxy nanocomposites," *Mater. Today Proc.*, vol. 44, pp. 346–355, 2021, doi: https://doi.org/10.1016/j.matpr.2020.09.742.

[4] H. Gu *et al.*, "An overview of multifunctional epoxy nanocomposites," *J Mater Chem C*, vol. 4, no. 25, pp. 5890–5906, 2016, doi: 10.1039/C6TC01210H.

[5] M. A. Ashraf, W. Peng, Y. Zare, and K. Y. Rhee, "Effects of Size and Aggregation/Agglomeration of Nanoparticles on the Interfacial/Interphase Properties and Tensile Strength of Polymer Nanocomposites," *Nanoscale Res. Lett.*, vol. 13, no. 1, p. 214, Jul. 2018, doi: 10.1186/s11671-018-2624-0.

[6] E. Kontou, A. Christopoulos, P. Koralli, and D. E. Mouzakis, "The Effect of Silica Particle Size on the Mechanical Enhancement of Polymer Nanocomposites," *Nanomaterials*, vol. 13, no. 6, 2023, doi: 10.3390/nano13061095.

[7] H. Zhang *et al.*, "Effect of nanoparticle size on the mechanical properties of polymer nanocomposites," *Polymer*, vol. 252, p. 124944, 2022, doi: https://doi.org/10.1016/j.polymer.2022.124944.

[8] Y.-M. Choi, S.-A. Hwangbo, T. G. Lee, and Y.-B. Ham, "Effect of Particle Size on the Mechanical Properties of TiO2–Epoxy Nanocomposites," *Materials*, vol. 14, no. 11, 2021, doi: 10.3390/ma14112866.

[9] Y. Zhou, E. White, M. Hosur, and S. Jeelani, "Effect of particle size and weight fraction on the flexural strength and failure mode of TiO2 particles reinforced epoxy," *Mater. Lett.*, vol. 64, no. 7, pp. 806–809, 2010, doi: https://doi.org/10.1016/j.matlet.2010.01.016.

[10] R. Kumar *et al.*, "Effect of particle size and weight fraction of SiC on the mechanical, tribological, morphological, and structural properties of Al-5.6Zn-2.2Mg-1.3Cu composites using RSM:

fabrication, characterization, and modelling," *Heliyon*, vol. 8, no. 9, p. e10602, 2022, doi: https://doi.org/10.1016/j.heliyon.2022.e10602.

[11] S.-Y. Fu, X.-Q. Feng, B. Lauke, and Y.-W. Mai, "Effects of particle size, particle/matrix interface adhesion and particle loading on mechanical properties of particulate–polymer composites," *Compos. Part B Eng.*, vol. 39, no. 6, pp. 933–961, 2008, doi: https://doi.org/10.1016/j.compositesb.2008.01.002.

[12] S. K. Singh, D. Singh, A. Kumar, and A. Jain, "An Analysis of Mechanical and Viscoelastic Behaviour of Nano-SiO2 Dispersed Epoxy Composites," *Silicon*, vol. 12, no. 10, pp. 2465–2477, Oct. 2020, doi: 10.1007/s12633-019-00335-x.

[13] A. Filippov, V. Fomin, I. Veretennikova, and S. Smirmov, "Investigation of elastic modulus of heterogeneous materials based on epoxy resin filled with silicon dioxide nanoparticles by nanoindentation," in *AIP Conference Proceedings*, Dec. 2020, p. 020094. doi: 10.1063/5.0034462.

[14] D. Soni, A. K. Sharma, M. Narwariya, and P. S. Chauhan, "Effect of Low Weight Fraction of Nano-reinforcement on Tensile Properties of Polymer Nanocomposites," in *Recent Advances in Mechanical Engineering*, M. Muzammil, A. Chandra, P. K. Kankar, and H. Kumar, Eds., Singapore: Springer Singapore, 2021, pp. 729–735.

[15] Y. Hua, L. Gu, S. Premaraj, and X. Zhang, "Role of Interphase in the Mechanical Behavior of Silica/Epoxy Resin Nanocomposites," *Materials*, vol. 8, no. 6, pp. 3519–3531, 2015, doi: 10.3390/ma8063519.

[16] M. Battistella, M. Cascione, B. Fiedler, M. H. G. Wichmann, M. Quaresimin, and K. Schulte, "Fracture behaviour of fumed silica/epoxy nanocomposites," *Compos. Part Appl. Sci. Manuf.*, vol. 39, no. 12, pp. 1851–1858, 2008, doi: https://doi.org/10.1016/j.compositesa.2008.09.010.

[17] M. S. Islam, R. Masoodi, and H. Rostami, "The Effect of Nanoparticles Percentage on Mechanical Behavior of Silica-Epoxy Nanocomposites," *J. Nanosci.*, vol. 2013, p. 275037, Dec. 2013, doi: 10.1155/2013/275037.

[18] S. Liu and T. Xia, "Continued Efforts on Nanomaterial-Environmental Health and Safety Is Critical to Maintain Sustainable Growth of Nanoindustry," *Small*, vol. 16, no. 21, p. 2000603, 2020, doi: https://doi.org/10.1002/smll.202000603.

[19] A. International, *ASTM D638-14, Standard Test Method for Tensile Properties of Plastics*. ASTM International, 2015. [Online]. Available: https://books.google.com/books?id=T0vBuQEACAAJ

[20] N. C. W. Judd and W. W. Wright, "VOIDS AND THEIR EFFECTS ON THE MECHANICAL PROPERTIES OF COMPOSITES - AN APPRAISAL.," *SAMPE Journal*, vol. 14, no. 1. pp. 10–14, 1978.

[21] A. I. Dmitriev, I. Häusler, W. Österle, B. Wetzel, and G. Zhang, "Modeling of the stress–strain behavior of an epoxy-based nanocomposite filled with silica nanoparticles," *Mater. Des.*, vol. 89, pp. 950–956, 2016, doi: https://doi.org/10.1016/j.matdes.2015.10.038.

[22] Q. Chen, I. Chasiotis, C. Chen, and A. Roy, "Nanoscale and effective mechanical behavior and fracture of silica nanocomposites," *Compos. Sci. Technol.*, vol. 68, no. 15, pp. 3137–3144, 2008, doi: https://doi.org/10.1016/j.compscitech.2008.07.013.

[23] F. Bondioli, V. Cannillo, E. Fabbri, and M. Messori, "Epoxy-silica nanocomposites: Preparation, experimental characterization, and modeling," *J. Appl. Polym. Sci.*, vol. 97, no. 6, pp. 2382–2386, 2005, doi: https://doi.org/10.1002/app.21854.

[24] M. Zamanian, F. Ashenai Ghasemi, and M. Mortezaei, "Interphase characterization and modeling of tensile modulus in epoxy/silica nanocomposites," *J. Appl. Polym. Sci.*, vol. 138, no. 5, p. 49755, 2021, doi: https://doi.org/10.1002/app.49755.

Author Biographies

Dr. Ryan Masoudi is an Associate Professor of Engineering at Thomas Jefferson University in Philadelphia, Pennsylvania. He received his PhD in Mechanical Engineering from the University of Wisconsin–Milwaukee. His research focuses on wicking and transport phenomena in porous media, thermal-fluid sciences, and composite materials, with an emphasis on sustainability and nanoscience. Dr. Masoodi is the co-editor of the forthcoming book *Wicking of Liquids in Porous Media: Advances and Applications* and serves on the editorial board of the *Capillarity*

Parinaz Heydar is a graduate student in the School of Design and Engineering at Thomas Jefferson University. Her research is focused on nanostructured materials, with a particular interest in SEM characterization techniques and 2D materials.

Md Saiful Islam is a Senior Material Innovator at Carhartt with over six years of experience in material innovation and R&D. He holds a Master of Engineering in Textile Sciences and Engineering from Philadelphia University, with expertise in fiber materials, material characterization, and fabric development.

International Journal of Energy Efficiency Engineering (IJEEE)
Volume 1, Issue 1 (May 2025), pages 48-64

INTERNATIONAL JOURNAL OF
ENERGY EFFICIENCY ENGINEERING

Effects of Uncertainty on the Prediction of Energy Consumption of Compressed Air Systems

Mohamed Elkholy[a1], Amin Esmaeili[b], and Javad Khazaii[c]

[a] Department of Mechanical Engineering, Kennesaw State University, Georgia, USA
[b] Department of Industrial and Systems Engineering, Kennesaw State University, Georgia, USA
[c] Department of Engineering Technology, Kennesaw State University, Georgia, USA

Abstract

Compressed air is an essential part of operations at many industrial and manufacturing plants. For example, compressed air can be used for stamping, clamping, driving power tools, cleaning tools, and powering controls or actuators. Simulink is used to model a continuously operating compressed air system, aftercooler, and heat-rejection system. The three main sources of energy consumed by the system include the energy consumed by the air compressor's motor, the energy consumed by the aftercooler's pump, and the energy consumed by the heat-rejection system's fan motor. Testing agencies test equipment per a standard and document performance results. Regulatory-governmental-agencies select a testing standard and a minimum performance rating. Regulatory agencies allow the manufacturers to advertise and sell their products if, during testing, product performance stays within an allowable tolerance. A typical acceptable tolerance for compressor airflow is between ± 4% and ± 7%, depending on the compressor's capacity,

[1] Corresponding Author: Mohamed Elkholy, engmohamedelkholy@yahoo.com

meanwhile, according to the ASHRAE 90.1, section G, the typical acceptable tolerance for the pump's waterflow rate is ± 5% of its rated value. Finally, the acceptable fan tolerance is between ± 3% and ± 5% of its rated value. Also, all other equipment in the plant has its own designated tolerances. These tolerances introduce uncertainty in predicting the overall system's energy consumption. The authors have used the compressor airflow's allowable tolerance in their compressed air model to evaluate the effects of this uncertainty on a compressed air system's predicted yearly energy consumption.

Keywords: *Compressed air systems; energy consumption; energy efficiency; energy saving; simulation modeling; Simulink.*

I. INTRODUCTION

Compressed air systems are one of the most important systems in the operations at many industrial and manufacturing facilities across various industries. Energy management and how to effectively deal with it in general have become important in recent years. It has been found that most of the energy consumption and energy waste inside these facilities takes place in the compressed air systems. It has also been found, during energy-assessment activities for the Industrial Training and Assessment Center (ITAC) of the United States Department of Energy that the majority of energy savings that achieved for various industrial facilities has come in from making their compressed air systems more efficient [1-3].

Because of that reality, a longtime topic of interest has been predicting these systems' energy consumption. Numerous articles and research papers have been published with the goal of both shedding more light on this subject and educating facility and maintenance engineers, helping them to better understand their compressed air systems and how to manage and maintain these systems during operations most effectively. These publications have also been critical to helping these personnel maximize the energy efficiency and productivity of their compressed air systems during operations. These publications also helped them increase performance, productivity, and be more efficient in energy consumption and achieve energy efficiency. Maxwell and Rivera [4] have focused on developing dynamic system modeling, running different energy-use simulations to provide an analytical tool for evaluating the performance of these systems under a variety of

operating conditions and control strategies. Schmidt and Kissock [5] estimated energy savings from energy conservation retrofits in compressed air systems from air use reduction and other changes. Thabet et al. [6] introduced the idea of using intelligent systems to reduce energy consumption and increase efficiency in compressors by considering real-time circumstances, artificial intelligence (AI), and predicted needs. Widayati and Nuzahar [7] conducted a research within the food industry explaining a technique for compressed air system optimization that determines the optimal conditions for compressors operation, while also evaluating energy needs to improve operating efficiencies, increasing energy savings and lowering costs. Schmidt and Kissock [8] presented a methodology that featured case-study examples, using easily obtainable performance data and rule-of-thumb methods, for modeling air compressor performance to calculate the projected energy savings. Hernandez-Herrera et al. [9] analyzed and calculated several main energy efficiency measures that can be applied to compressed air systems as necessary tools for companies that want to reduce energy consumption. Hessmer et al. [10] provided comprehensive information complied from technical reviews and scoping studies carried out at industrial facilities, in which energy efficiency upgrades had been made to the compressed air systems. Mousavi et al. [11] presented an overview of techniques used to model energy consumption as well as various approaches to controlling compressed air systems and to demonstrating the system's energy consumption dynamics.

In this research, the authors take a novel approach in predicting overall energy consumption for compressed air systems in manufacturing facilities. According to the U.S. Department of Energy's test procedures for compressor final rule (DOE 2016, 216) [12], a typical acceptable tolerance for compressor airflow is between ± 4% and ± 7%, depending on the compressor's capacity. According to ASHRAE 90.1, section G (ASHRAE 2019) [13], the typical acceptable tolerance for the pump's waterflow rate is ± 5% of its rated value. Finally, the acceptable fan tolerance is between ± 3% and ± 5% of its rated value (AHRI 2016, 4) [14]. Also, all other equipment in the plant has its own designated tolerances. Usually, these tolerances are not taken into consideration when predicting energy consumption within a feasibility or scope studies pertaining to the installation of any new project or when predicting operational costs for a given industrial facility. In this research, the authors study the effects of uncertainty on the airflow of compressed air systems across a year. A compressed air system model was developed and employed utilizing MATLAB Simulink, to evaluate its impacts in predicting total energy consumption and costs for

the integral compressed air system. The hourly temperature variation across all of 2021 in Atlanta, Georgia, USA, was also considered, to optimally predict total energy consumption for the entire system per annum based on an hourly study. The results of this study will help different stakeholders and managers develop accurate studies to better estimate costs when they want to install a new system or upgrade an existing one. It provides a way to help facility managers more accurately predict energy consumption for their compressed air systems.

II. COMPRESSED AIR SYSTEM MODEL

In this paper, a simulation for a compressed air system model was developed utilizing MATLAB Simulink based on thermodynamics, heat transfer, and fluid mechanics theories. A visualization of a real compressed air system of a certain industrial process that requires a steady amount of 0.5 kg/sec supply of compressed air at a required pressure of 500 kPa and a maximum temperature of 30 °C was prepared at the beginning. This compressed air system consists of a) an Isentropic compressor with an efficiency of 80 % that compresses a certain amount of air at local ambient conditions (100 kPa pressure, and current ambient temperatures) into the required operating pressure, b) a cooler acting as a cross-flow heat exchanger to reduce the temperature of the air merging from the compressor to no higher than the required maximum temperature of 30 °C in the system, c) a water pump that provides the required amount of cooling water, from a cooling tower, needed for the heat-exchange process, and d) a cooling tower that reduces the temperature of the hot water emerging from the heat exchanger post-heat-exchange process. Figure 1 below shows visualization of the compressed air system, including its various components.

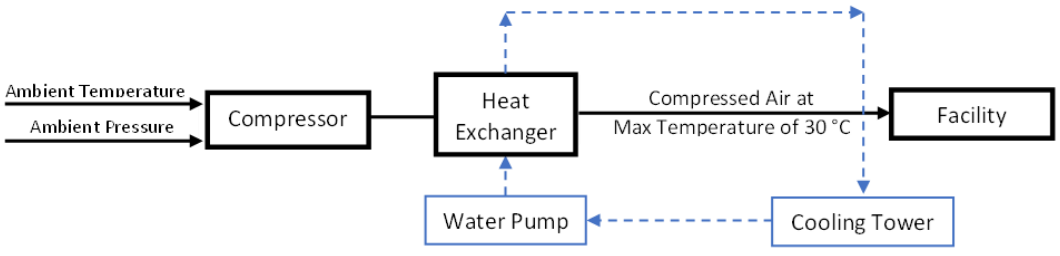

Figure 1: Visualization of the compressed air system used in the simulation.

Modeling for the compressed air system consists of engineering formulas and mathematical equations that build the system and connect its various components, as explained later in this paper.

Each physical component in the above compressed air system visualization was modeled using several blocks in SIMULINK.

In the SIMULINK modeling, each block performs a specific process. The blocks are also arranged in the same order as the flow of mathematical equations used to solve the engineering formulas that render the results for each physical component (compressor, heat exchanger, water pump, and cooling tower) within the integral compressed air system. Each block in the model has input and output data; these sets of input data represent numbers tied to each physical component in the compressed air system or pull from results from the previous operation of the model, while the output data are the results of the specific processes of each block in Simulink.

A. Compressor Model

The air compressor modeling begins by identifying the thermodynamic operations required to obtain the required operating pressure of 500 kPa and the actual temperature leaving the compressor. Fundamental equations governing these operations are shown in Eqs. (1) to (5). The ambient atmospheric pressure of 100 kPa represents these equations' first input data. The second input data represent the acceptable mass flow rates of the air that would be compressed by the compressor. The last input data are the ambient temperatures. In this paper, the actual variation of ambient temperature per hour throughout the year of 2021 were used rather than assuming a fixed or input temperature at any moment. Detailed temperature data for Atlanta, Georgia, USA, for every hour of the normal business day (8:00 a.m.-8:00 p.m.) in 2021 of most of the area's industrial facilities were obtained from the World Weather website [15] and were used as input data for the fundamental mathematical equations governing the entire model during simulations.

$$T_{2s} = T_1 \left(\frac{P_2}{P_1}\right)^{\frac{k-1}{\kappa}} \tag{1}$$

$$W_{cs} = C_p(T_1 - T_{2s}) \tag{2}$$

$$\eta_s = \frac{W_{cs}}{W_c} \text{ so that } W_c = \frac{W_{cs}}{\eta_s} \tag{3}$$

$$\dot{W} = \dot{m}\, W_c \tag{4}$$

$$W_C = \dot{m} C_p (T_1 - T_2) \tag{5}$$

where:

P_1: Input ambient pressure.

P_2: The required operating pressure.

T_1: The hourly input temperatures.

T_2: The actual temperature leaving the compressor.

$\dot{W}$: Power required to drive the compressor.

These equations are modeled using SIMULINK blocks in the correct order to model the compressor component's performance only within the integral compressed air system.

B. Heat Exchanger Model

Since air is coming out from the compressor at a high temperature, an effective cooling process through a suitable heat exchanger is necessary to reduce this temperature and maintain a maximum operating temperature of 30 °C, for safe operations within the facility. A suitable cross flow heat exchanger that uses coolant water has been selected for the cooling process. This heat exchanger has a surface area of 240 m², a heat transfer coefficient (U) of 225 W/m²·k., and an efficiency (Є) of 94 %. Cooling water enters the heat exchanger at 16° C with a c_p of 4.186 kJ/kg·K, and it will be cooled down using a cooling tower and an appropriate water pump after emerging from the heat exchanger at a high temperature. Our heat exchanger modeling began by identifying the heat transfer operations required to design an effective heat exchanger. The fundamental relations governing these operations are shown below:

Step 1: Determining $C_{\min}$ between $C_{air} = \dot{m}\, c_p$ of air and $C_{water} = \dot{m}\, c_p$ of the cooling water (6);

Step 2: Using a heat exchanger efficiency (Є) of 94 %;

Step 3: Calculating $q_{act} = \epsilon \times C_{\min} \times (T_{hi} - T_{ci})$ to get the heat transfer rate between the entering hot air emerging from the compressor and the entering cold water to the heat exchanger (7); and

Step 4: Using the same heat transfer rate calculated from Step 3 to calculate the air temperature leaving the compressor ($\boldsymbol{T_{ho}}$) from Eq. (8):

$$q_{act} = \epsilon \times C_{\min} \times (T_{hi} - \boldsymbol{T_{ho}}) \quad (8)$$

These steps are modeled later using SIMULINK blocks in the order to model the compressor component only within the entire compressed air system.

C. Open-Circuit Heat-Rejection Model and Total Power Required for the System

It is necessary to provide the system with a cooling tower and a water pump to keep the cooling water used in the heat-exchange process low, at 16° C, after it emerges from the heat exchanger. An efficient cooling tower and an appropriate water pump were selected to achieve this process after doing the required calculations for the cooling capacity needed. The actual heat to be removed from the air compressor by the heat exchanger was obtained at the beginning from Step 4. According to ASHRAE 90.1, section G.3.1.3.11 (ASHRAE 2019, 317) [13], any open-circuit heat-rejection system works between 83° F and 93° F (33.9° C and 28.3° C) as a standard operation set point with ΔT_{water} = 5.6 °C. The mass-flow rate of cooling water used in the heat-rejection system, $\dot{m}_{water}$, with the unit of kg/sec was subsequently calculated from the following equation:

$$\dot{m}_{water} = \frac{\dot{Q}_{water} \; or \; q_{act}}{c_{p-water} \cdot \Delta T_{water}} \quad (9)$$

Then the $\dot{m}_{water}$ was converted to GPM. Based on section G3.1.3.11 of ASHARAE 90.1 (ASHRAE 2019, 317) [13], the maximum fan power for heat-rejection equipment shall have an efficiency of 38.2 gpm/hp. Therefore, the fan power, P_{fan}, was subsequently calculated from Eq. (10):

$$P_{fan} = \frac{\dot{m}_{water}}{38.2} \quad (10)$$

Based on the same section of the ASHRAE 90.1 (ASHRAE 2019, 317) [13], the maximum pump power input should be 19 W/gpm. Therefore, the total pump power, P_{pump}, was calculated based on Eq. (11),

$$P_{pump} = 19 \, \dot{m}_{water} \quad (11)$$

Modeling for the open-circuit heat-rejection system was performed based on these functions on SIMULINK. Meanwhile, total power required for the integral compressed air system was easy to predict from the final modeling on SIMULINK, based on the power required to drive the compressor (5), the fan power required in (10), and the total pump power (11).

III. COMPRESSED AIR SYSTEM SIMULATION

A reliable model, which would later be effectively utilized, was prepared for the next phase of simulations and results. According to Table 1 in the U.S. Department of Energy's test procedures for compressor final rule (DOE 2016, 216) [12], a typical acceptable tolerance for compressor airflow of is between ± 4% and ± 7%, depending on the compressor's capacity. It was found, based on the current mass flowrate of air ($\dot{m} = 0.5\ \text{kg/s} = 415.28 \times 10^{-3}\ \text{m}^3\ /\ \text{sec}$) utilized in this research, that the acceptable tolerance in airflow is ± 4%. A simulation in Simulink has been run on 25 different random values of the ($\dot{m}$) in a range of ± 4 %. MS Excel's "Random" function was used between 0.48 kg/s and 0.52 kg/s to get the 25 random values of $\dot{m}$. These values were then used in the simulation phase on SIMULINK to find total power consumed by the integral compressed air system for each random value of $\dot{m}$. The total power consumption values based on the random values of $\dot{m}$ and based on the variation of actual ambient temperatures from 8:00 am to 8:00 pm across all of 2021 were recorded. The total power consumption of the integrated compressed air system for each value of ($\dot{m}$) of air used in the simulation represents a total of the power required by the compressor to achieve operation, the power used by the cooling tower fan, and the power used by the cooling power pump. Figure 2 shows an example of total power consumed by the integral system on SIMULINK when a random value of 0.495 kg/s for airflow rate ($\dot{m}$) was utilized for a simulation from 8:00 a.m. to 8:00 p.m. throughout 2021. In the figure, the X-axis represents the normal workday hours of 8:00 a.m. to 8:00 p.m., while the Y-axis represents the total power consumed by the entire system in (kW), and each curve represents total hourly power consumption across all 12 months of 2021.

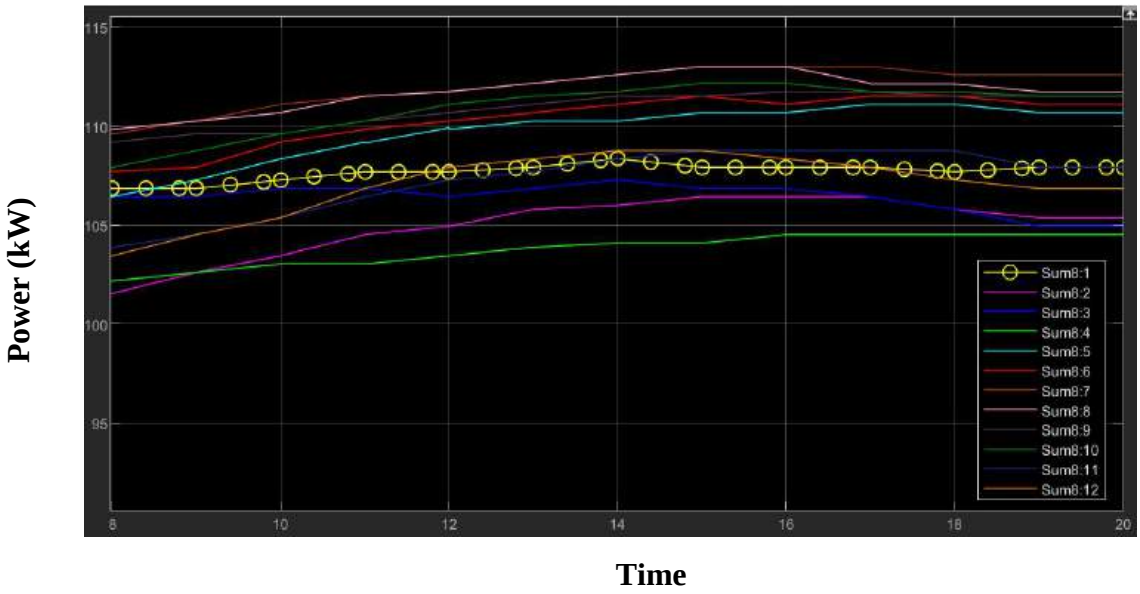

Figure 2: Total power consumption for the whole system for $\dot{m}$ = 0.495 kg/s on Simulink.

Curves values were imported after that by MATLAB to an Excel spreadsheet to calculate the summation value of the total power consumption of each hour across the year. The total power consumption for this simulation in 2021 was found to be 515,234.17 kWh/yr. The same operation was performed for the other 24 random values of the mass-flow rate of air to get a set of results for the integral system's total power consumption.

IV. SIMULATION RESULTS AND ANALYSIS

A set of results pertaining to total power consumption in the integral system, based on simulations of the 25 random values of the mass-flow rate of air were collected. An analysis was performed after that via Excel by generating a bell curve for these results, initially calculating the Mean value, Standard Deviation value, and then the Normal Z-Distribution values. The bell curve was generated based on the total power-consumption values per year (kWh/yr) for the results obtained from the simulation and the Normal Z-Distribution values for each result. Figure 3 below shows the aforementioned bell curve.

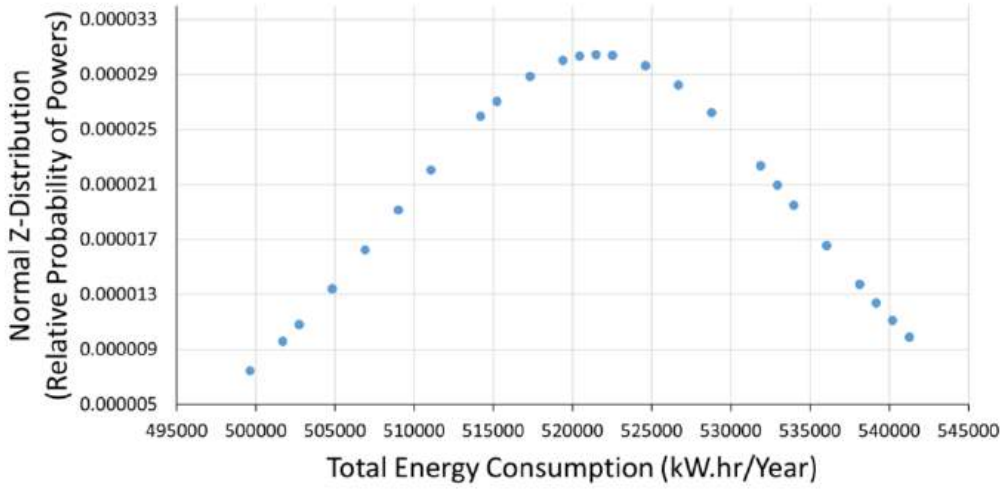

Figure 3: Bell curve for the simulations results.

It was found that the majority (68 percent) of the total power consumption values per year lie between 508,502 kWh/yr and 534,706 kWh/yr, 95 percent of the total power consumption values per year lie between 495,400 kWh/yr and 547,808 kWh/yr, and 99.7 percent of the total power consumption values per year lie between 482,298 kWh/yr and 560,910 kWh/yr. Figure 4 shows a histogram of the frequency of several total power consumption bins.

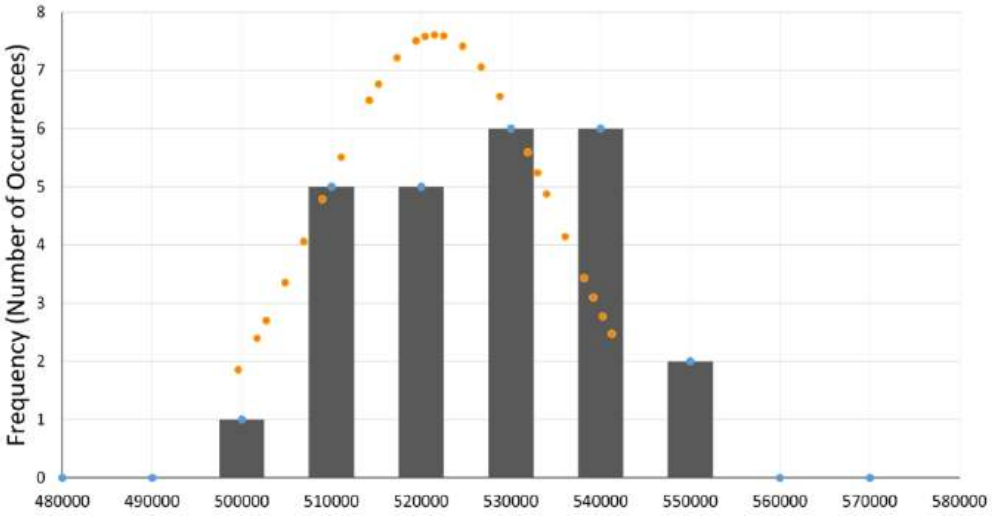

Figure 4: Histogram of the frequencies of several total power consumption bins.

Based on the number of occurrences shown in Figure 4, it was found that among the performed 25 random simulations, the majority of total power consumption possibilities occurred two times

in 530,000 kWh/yr and 540,000 kWh/yr, with 12 instances and a 48% possibility of occurrence; the total power consumption of 510,000 kWh/yr and 520,000 kWh/yr occurred 10 times, with a 40% possibility of occurrence; the total power consumption of 550,000 kWh/yr occurred 2 times, with an 8 percent possibility of occurrence; and the total power consumption of 500,000 kWh/yr occurred 1 time, with a 4% possibility of occurrence.

A. Additional Simulations and Analyses

In the previous section, authors used the parameter uncertainty for only one element of the system and simulated the whole year energy consumption of the system. In this section, the authors incorporated the effects of multiple elements uncertainties, but only simulated the instantaneous pick energy consumption. To do this, authors developed a MATLAB based simulation model and included the effects of more parameters uncertainty (outdoor temperature sensor tolerance, system operation temperature sensor tolerance, air and water flow capacity tolerances affecting the power consumption of the compressor, cooling tower fan and pump) in model when evaluating the energy consumption of the overall system. As it was noted earlier, this modeling is performed for the pick load condition instant only, but the intention here is to show not only the effects of different parameters uncertainty collectively, but to evaluate the effects of air leakage in the compressed air system on overall energy consumption of the system which is the main cause of energy loss in air compressed systems. The deterministic simulation is performed first in the MATLAB based simulation model (with no uncertainty considered) for the pick load condition with some specific inputs to the system. The results of this model showed the overall energy consumption of the system to be close to 111 kW. Another coding represented the simulation result (500 simulations) when the tolerances for the temperature sensors, and air and water flows are included in the model. The results as has been depicted in Figure 5 showed a possible total energy consumption range of 105 to 117 kW. The system energy consumption during the pick load, when there are 5% and 10% leaks in the system was performed as well. When there is 5% leak in the system, the overall energy consumption in pick instant, as it is shown in Figure 5, has a range of 111 to 123 kW. This represents a possibility of up to 12% energy loss (50% chance of 5.5% loss, and 25% chance of 7.5% loss) due to a 5% leak only. Finally, when there is a 10% air leak in the system, the overall energy consumption in pick instant has a range of 115.5 to 128 kW.

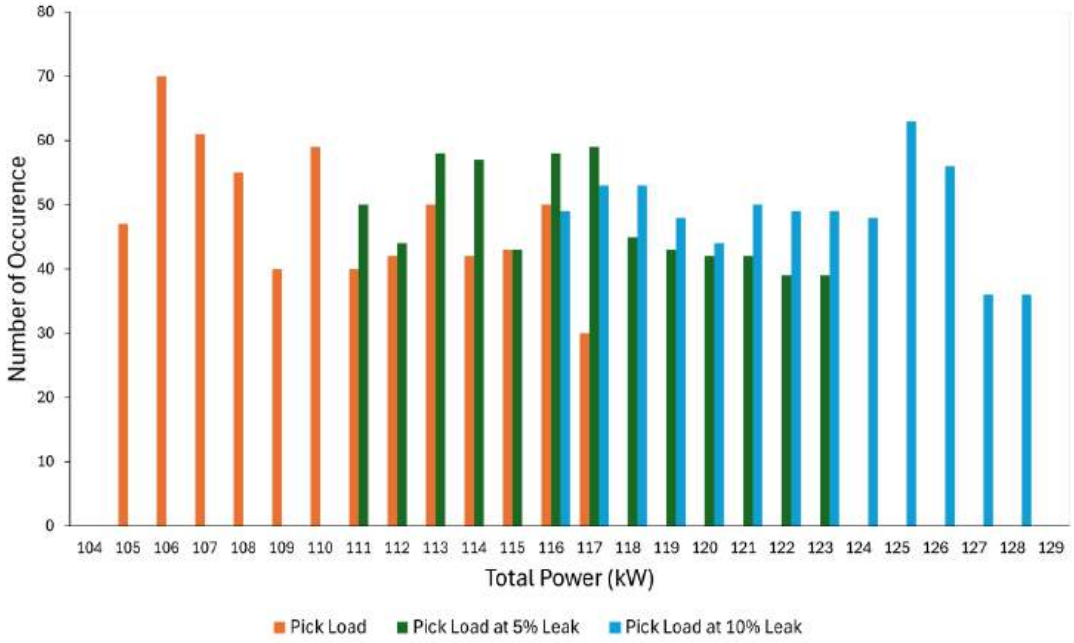

Figure 5: Histogram of the frequencies of total power consumption in 3 cases.

This, as it is shown in Figure 5, represents a possibility of up to 15% loss of energy due to a 10% leak (100% chance of 4% loss, 50% chance of 10% loss, and 31% chance of 12% loss).

V. CONCLUSION

A model for a compressed air system was prepared and then created on MATLAB Simulink. A set of simulations based on different random values within the allowable tolerance for a certain rated value of the mass-flow rate of air were run on Simulink for the created modeling. This rated value is 0.5 kg/sec, and the tolerance permitted for this value was found to be ± 4% (between 0.48 kg/sec and 0.52 kg/sec). It was found via simulation that the total power consumption in the compressed air system per year of the rated mass-flow rate of air (0.5 kg/sec) was 520,438 kWh/yr, but due to the allowable tolerance for the rated value of airflow into the compressor, we saw that the total consumption per the year can be any value between 499,621 kWh/yr and 541,256 kWh/yr. So, it was concluded that the total energy consumption of this compressor per year based on uncertainty in the air-flow rate to the compressor can vary across a remarkable range of 41,635 kWh/yr between 499,621 kWh/yr and 541,256 kWh/yr, instead of 520,438 kWh/yr. Also, modeling was done while multiple parameters uncertainty was

considered. Simulation represented similar outcomes. In addition, the effects of air leaks were evaluated on overall energy consumption of the system, pointing to major energy losses due to 5 to 10% leaks only. Allowable tolerance in the mass-flow rate of the air used in air compressors can cause a considerable range of possible power consumption instead of only one calculated value, and that these tolerances are the source of uncertainty when predicting a compressed air system's total yearly energy consumption. To accurately predict total energy consumption, plant design and energy engineers designing any facility with air compressors should consider these tolerances in their calculations when predicting a compressed air system's total energy consumption, instead of depending only on one value for the mass-flow rate of air. In this paper, the authors proved - based on modeling and the simulation of a real compressed air system of a certain industrial process - that uncertainty has a remarkable effect on total energy consumption. They explained in detail a general method and provided a useful technique that can be employed for any compressed air system to predict the system's total energy consumption while also considering the uncertainty resultant from allowable tolerances in the air-flow rates. One important finding here is that a decrease in allowable manufacturing tolerances could contribute to reducing uncertainty and therefore rendering greater energy savings. Another important finding is that the authors have shown that only one unknown factor (e.g., equipment-test tolerance allowance) can contribute to 2.5% to 4% of uncertainty within a system's overall energy consumption. Given that guideline state that the allowable tolerances for airflow entering the compressor is 4% to 7% for different quantities of airflow, it can be seen that the uncertainty within the system's overall energy consumption can actually be even higher than the predicted 2.5% to 4% found here.

V. Future Work

The created compressed air modeling in this report can be implemented in many other research-based projects and experiences as well. The authors plan to use it in identifying other variables and changes that occur within integral compressed air systems and to study the effects of uncertainty resultant from these variables when predicting a compressed air system's energy consumption. The modeling can also be used to check the effects of the air leakages that take place when operating compressed air systems within industrial facilities. The produced air

pressure used in this current research can also be modified within a specific range – say, to that of the operational ranges used in most facilities – to study how changing the inputs affects the outputs of compressed air systems. A lot of research ideas and expansion can be performed using this current model and based on the results of this research in the future, manufacturers and engineers at industrial facilities will be able to better increase their compressed air system's efficiency and performance, predict actual total energy consumption, and increase the system's energy efficiency. As noted earlier, the authors have evaluated the effects of uncertainty pertaining to the volumetric airflow quantity entering the air compressor on a typical compressed air system's overall energy consumption. The authors have shown that the permitted tolerances given by the regulatory standards based on manufacturers' testing structures can contribute to uncertainty when predicting the overall system's energy consumption. Of course, uncertainty can be generated from different (other) sources/equipment as well, and their inclusion would help us more accurately model energy consumption. As mentioned throughout the paper, the authors have only focused on only one uncertainty parameter (the quantity of compressed airflow) in developing this model. This model can be considerably improved by introducing the uncertainty parameter of other (more) equipment designated for usage in the overall plant. Such work would allow the user to perform a greater number of evaluations, such as sensitivity analysis, and point out which equipment is having the most profound impact on the plant's overall energy consumption.

References

[1] The Industrial Assessment Centers (IAC) of the U.S. Department of Energy, "*Centers: Kennesaw State | KS."* Accessed November 24, 2022. https://iac.university/center/KS

[2] The Industrial Assessment Centers (IAC) of the U.S. Department of Energy, "*Database: Search: Assessments: Kennesaw state."* Accessed November 24, 2022. https://iac.university/searchAssessments?center=KS&state

[3] The Industrial Assessment Centers (IAC) of the U.S. Department of Energy, "*Database: Search: Assessments."* Accessed November 24, 2022. https://iac.university/searchAssessments

[4] G. Maxwell, and P. Rivera, "Dynamic simulation of compressed air systems," *ACEEE Summer Study on Energy Efficiency in Industry*, pp. 146-156, 2003.

https://www.eceee.org/library/conference_proceedings/ACEEE_industry/2003/Panel_3/p3_14/

[5] J. K. Kissock, and C. Schmidt, "Modeling and simulation of air compressor energy use," *ACEEE Summer Study on Energy Efficiency in Industry*, vol. 1, no. 13, pp. 131-142, 2005. https://academic.udayton.edu/kissock/http/Publications/AirSim_ACEEE2005.pdf

[6] M. Thabet, D. Sanders, V. Becerra, G. Tewkesbury, M. Haddad, and T. Barker, "Intelligent energy management of compressed air systems, " *2020 IEEE 10th International Conference on Intelligent Systems (IS)*, pp. 153-158, 2020. doi: 10.1109/IS48319.2020.9199977.

[7] E. Widayati, and H. Nuzahar, "Compressed Air System Optimization: Case Study Food Industry in Indonesia," *IOP Conference Series: Materials Science and Engineering*, vol. 105, no. 1, p. 012018, 2016. doi: 10.1088/1757-899X/105/1/012018.

[8] C. Schmidt, and J. K. Kissock, "Estimating energy savings in compressed air systems,'' *Mechanical and Aerospace Engineering Faculty Publications*., 145, 2004. https://ecommons.udayton.edu/mee_fac_pub/145

[9] H. Hernandez-Herrera, et al., "Energy Savings Measures in Compressed Air Systems," *International Journal of Energy Economics and Policy.*, vol. 10, no. 3, pp. 414-422, 2020,. doi: 10.32479/ijeep.9059.

[10] C. Hessmer, J. Olmsted, S. Meserve, and R. K. Kondapi, "Compressed Air System Energy Efficiency Upgrades Implemented vs. Underutilized Measures," ACEEE Summer Study on Energy Efficiency in Industry conference, 2015. https://www.aceee.org/files/proceedings/2015/data/papers/4-15.pdf

[11] S. Mousavi, S. Kara, and B. Kornfeld, "Energy efficiency of compressed air systems," *Procedia Cirp*., vol. 15, pp. 313-318, 2014. doi: 10.1016/j.procir.2014.06.026.

[12] U.S. Department of Energy (DOE), "*Energy Conservation Program: Test Procedures for Compressors."* Published May 5, 2016 at Office of Energy Efficiency and Renewable Energy, Department of Energy. https://www.energy.gov/sites/prod/files/2016/12/f34/Compressors%20TP_FR_12-1-16_Final%20Issuance%20CLN%20v2.pdf

[13] American Society of Heating, Refrigerating and Air-Conditioning Engineers (ASHRAE). 2019. "ASHRAE Standard 90.1: Energy Standard for Buildings Except Low-Rise

Residential Buildings: Section G" Accessed October 20, 2022. https://ashrae.iwrapper.com/ASHRAE_PREVIEW_ONLY_STANDARDS/STD_90.1_2019.

[14] Air-Conditioning, Heating, and Refrigeration Institute (AHRI). 2016. *"AHRI Standard 420 (I-P): Standard for Performance Rating of Forced-circulation Free-delivery Unit Coolers for Refrigeration: Section 5.3."* Accessed October 28, 2022. https://www.ahrinet.org/sites/default/files/2022-06/AHRI_Standard_420_I-P_2016.pdf .

[15] World-Weather.info, "World: United States: Georgia: Weather in Atlanta." Accessed October 20, 2022. https://world-weather.info/forecast/usa/atlanta_1/january-2021/

Author Biographies

Mohamed Elkholy is a former graduate research assistant and master's student at Kennesaw State University and a former Lead student at the Georgia Industrial Training and Assessment Center. He is an experienced mechanical engineer in mechanical design and construction, HVAC, firefighting, plumbing, project management, LEED, energy assessments, compressed air, mechanical inspections, TAB, and code compliance.

Dr. Amin Esmaeili is the director of the Georgia Industrial Training and Assessment Center (Geo-ITAC) and associate professor of industrial and system engineering at KSU. Since 2021, he has led the Geo-ITAC team in conducting *energy, productivity, and sustainability assessments* for small- and medium-sized industrial facilities across Georgia through funding provided by the U.S. Department of Energy (DOE).

Dr. Javad Khazaii is an associate professor of mechanical engineering technology at Kennesaw State University (KSU). He has co-authored scientific articles and conference proceedings for the ASME and IBPSA. He is ranked 31st among academic scholars (lifetime) in the world in the field of "Heating, Ventilation, and Air Conditioning" by ScholarGPS in 2024.

International Journal of Energy Efficiency Engineering (IJEEE)
Volume 1, Issue 1 (May 2025), Pages 65-93

INTERNATIONAL JOURNAL OF
ENERGY EFFICIENCY ENGINEERING

Design and Optimization of a Lab-Scale System for Efficient Green Hydrogen Production Using Solar Energy

Hamza Alnawafah, Qais Alnawafah, Omar Al Sotary, Ryoichi S Amano[1]

Department of Mechanical Engineering, University of Wisconsin-Milwaukee 115 E. Reindl Way, Glendale, WI 53212

ABSTRACT

This paper presents the design and optimization of a novel lab-scale green hydrogen production system driven by solar photovoltaic (PV) energy. The primary focus is to enhance the efficiency of hydrogen production by addressing key challenges in electrical integration and power electronics. To achieve minimal power losses and maintain voltage and current levels within optimal operating parameters, advanced energy conversion techniques have been implemented. The system incorporates real-time control to dynamically synchronize PV output with electrolyzer requirements, maximizing production efficiency. Experimental results show that the system achieves a hydrogen production rate of up to 3.0 liters over 10 minutes at an optimal operating current range of 1.0–2.5 A, and an input voltage range of 4.5–7.5 V. Compared to conventional systems, the setup demonstrated an 18% reduction in power losses and a 25% improvement in operational stability under fluctuating irradiance conditions. The integration of battery

[1] Corresponding Author: Professor Ryoichi Amano: amano@uwm.edu

storage and a solar emulator further supports consistent performance, making the system a promising model for scalable, renewable hydrogen generation. While this work primarily evaluates hydrogen production, oxygen was also generated in a 2:1 molar ratio and released, with future work aimed at capturing and utilizing this byproduct.

Keywords: Green hydrogen; solar electrolysis; PV integration; power electronics; energy efficiency.

I. INTRODUCTION

Solar energy, harvested from the sun's abundant and renewable radiation, is an unlimited and sustainable energy resource. Technological advancements have greatly enhanced the efficiency of capturing and converting solar energy into usable forms, establishing solar power as a key component in the clean energy transition. This section discusses the core principles, applications, and emerging innovations in solar technologies. The renewable and eco-friendly characteristics of solar energy make it a critical alternative to conventional fossil fuels, addressing the global demand for clean energy while mitigating climate change [1]. Solar photovoltaic (PV) systems have emerged as a leading solution due to their increased efficiency and cost-effectiveness in converting sunlight directly into electricity [2].

Recent developments in building-applied photovoltaics (BAPV) and building-integrated photovoltaics (BIPV) highlight their dual roles in power generation and architectural integration, enhancing both energy efficiency and building aesthetics [3]. Similarly, solar thermal technologies for heating, cooling, and thermal energy storage are gaining recognition for their role in low-carbon buildings [4]. Emerging trends focus on scalable and adaptable PV systems, including floating PV arrays and large-scale ground-mounted solar power plants, which demonstrate significant potential in diverse environments [5]. Additionally, vehicle-integrated photovoltaics (VIPV) are gaining traction due to their applications in the automotive sector, expanding the scope of solar energy usage [6]. Crystalline silicon (c-Si) solar cells dominate the market due to their high efficiency,

affordability, and environmental safety [7]. Furthermore, photovoltaic monitoring systems (PVMS) are essential for maintaining system performance, offering real-time data and enabling predictive maintenance [8]. The integration of digital technologies, including the Internet of Things (IoT) and Big Data analytics, has revolutionized solar energy systems by improving operational efficiency, monitoring, and maintenance [9]. Policy frameworks and economic incentives play a crucial role in driving solar energy adoption. Governments worldwide have implemented policies promoting renewable energy to support sustainability, economic development, and environmental conservation [10]. Advancements in energy storage systems complement the growth of solar technologies by addressing the intermittent nature of solar energy. Enhanced battery storage solutions improve grid integration, reliability, and overall system stability [11].

The integration of solar energy into the transportation and industrial sectors is significantly advancing decarbonization strategies. In transportation, the deployment of solar-enabled infrastructure—such as electric vehicle (EV) charging stations and solar-assisted public transit systems—is experiencing accelerated growth [12]. VIPV embed solar modules directly onto vehicle surfaces, are being engineered to extend EV driving range and reduce reliance on conventional charging infrastructure [13]. Several urban centers have piloted solar-powered public transportation systems—such as buses and trains—highlighting their effectiveness in decreasing fossil fuel use [14]. Within the industrial sector, solar energy is being applied in both electricity generation and thermal applications. Energy-intensive industries, including manufacturing, textiles, and mining, are progressively implementing photovoltaic and solar thermal technologies to satisfy operational energy demands while simultaneously lowering emissions and cutting energy expenses [15]. Furthermore, utility-scale solar installations provide shared-access energy solutions, enabling industries to benefit from cost-efficient renewable power through centralized infrastructure and economies of scale [16]. Overall, integrating solar technologies across these domains strengthens energy resilience, promotes environmental sustainability, and fosters new economic development pathways.

Green hydrogen, generated via water electrolysis powered by renewable energy sources, is increasingly recognized as a pivotal solution in advancing low-carbon energy systems. As a clean, zero-emission fuel, it holds particular promise for decarbonizing sectors that are not easily electrified [17]. Ongoing enhancements in electrolyzer design—especially in proton exchange membrane (PEM) and alkaline systems—have significantly contributed to lowering production costs and boosting operational efficiency, thus improving the viability of large-scale deployment [18]. Research also indicates that improved durability and performance of electrolyzers are critical factors driving the advancement of green hydrogen technologies [19].

Policy support has been a major enabler of progress in this field. Strategic initiatives such as the European Union's Hydrogen Strategy, along with national programs in Germany and Japan, have directed substantial public funding and introduced incentives that are accelerating the adoption of green hydrogen technologies [20]. These frameworks are essential in developing infrastructure and market readiness for widespread implementation.

Nevertheless, green hydrogen still faces notable barriers, particularly in areas related to its storage, distribution, and transport. Its inherently low volumetric energy density poses challenges, requiring the development of advanced storage technologies that are both efficient and economically viable [21]. Furthermore, existing energy systems must be adapted to accommodate hydrogen, which may involve extensive infrastructure modifications [22]. Solving these issues is imperative for green hydrogen to achieve meaningful scale.

Due to its adaptability, green hydrogen is being investigated for diverse applications across sectors. In transportation, it is under consideration as a sustainable fuel for long-haul trucks, public transit, and aviation—contributing to reduced reliance on petroleum-based fuels [23]. In industrial operations, it is finding use as a low-emission feedstock in sectors such as ammonia production and steelmaking, helping to decarbonize processes traditionally associated with high carbon footprints [24].

Looking forward, the scalability of green hydrogen depends on continuous innovation in key technological domains. Advancements in electrolyzer efficiency, integration with renewable energy sources, and cost-effective hydrogen logistics are essential for expanding its role in the global energy mix. Interdisciplinary collaboration among policy-makers, researchers, and industry stakeholders will be vital to overcoming current limitations and driving broader adoption [25]. With its potential to support decarbonization goals and strengthen energy resilience, green hydrogen is positioned to be a cornerstone of future sustainable energy systems. Novel experimental setups, such as the capillary-fed electrolysis cells reported in recent studies, have demonstrated higher hydrogen production rates while minimizing energy losses [26]. The integration of acoustic stimulation in electrolysis, resulting in a 14-fold increase in efficiency, highlights a novel mechanism for enhancing hydrogen evolution reactions under neutral pH conditions [28].

Additionally, a groundbreaking membrane-based seawater electrolyzer has emerged as a cost-effective solution by eliminating the need for energy-intensive pre-desalination processes, making it ideal for coastal applications [27]. These innovations address critical challenges related to feedstock availability, energy efficiency, and scalability, positioning green hydrogen as a viable alternative to conventional hydrogen sources. Green hydrogen, produced through the electrolysis of water using renewable energy sources, has emerged as a key component in the transition to sustainable energy systems. However, many existing experimental studies focus either on large-scale installations or theoretical simulations and often lack a practical, reproducible lab-scale platform for testing the integration of PV and electrolysis systems. Challenges such as inconsistent solar irradiance, lack of real-time control, and inefficient power transfer still hinder optimal hydrogen production at small scales. Moreover, most existing systems do not account for the need to simulate solar conditions indoors or adjust PV output dynamically based on electrolyzer behavior.

This paper addresses these limitations by presenting a novel, modular lab-scale green hydrogen production system that integrates PV panels, battery storage, real-time

monitoring, and a programmable solar emulator. The system is designed to operate flexibly under both simulated and natural sunlight, with a decentralized control mechanism ensuring optimal voltage and current delivery to the electrolyzer.

The novelty of this work lies in its combined use of simulation-driven LED-based solar emulation, real-time power management, and experimental validation. This setup enables accurate performance characterization, improves operational stability, and supports scalable design concepts. The proposed platform bridges the gap between theoretical modeling and real-world implementation, serving as a foundation for future research and development in sustainable hydrogen production systems.

Fully renewable microgrids integrated with battery storage systems have been identified as a viable approach to producing green hydrogen efficiently. These microgrids encompass generation, transmission, distribution, and storage systems powered by renewable sources and are classified into DC microgrids, AC microgrids, and hybrid configurations based on their operational setup [29-30]. By leveraging PV emulators and advanced battery storage, microgrids mitigate the intermittent nature of solar power while ensuring a stable and continuous energy supply to the electrolyzer [29].

Experimental setups demonstrate the potential of such systems, with decentralized control ensuring optimal voltage and current conditions for hydrogen production. Recent research in lab-scale configurations integrating PV emulators and battery systems has shown promising results, improving power stability and reducing energy losses during electrolysis [30]. These innovations further establish microgrid-based hydrogen production as a scalable and modular solution for future renewable energy systems [31].

The main objective of this research is to design, develop, and optimize a scalable and modular lab-scale system for green hydrogen production by integrating PV emulators, battery storage, and decentralized control systems within renewable microgrids. The study

aims to address key challenges related to energy intermittency, efficiency losses, and system integration, providing an innovative framework for stable and cost-effective hydrogen production. By investigating advanced control mechanisms and power stabilization techniques, this research contributes to the development of scalable solutions that align with global sustainability goals and offer practical applications in industrial, transportation, and energy sectors.

II. MATERIALS AND METHODS

A. Experimental Setup Description

The experimental setup for green hydrogen production integrates key components for efficient operation, as illustrated in Figures 1 and 2. The system is divided into two main areas: the hydrogen generation system and the data acquisition section. The hydrogen generation begins with PV panels that convert solar energy into electrical power.

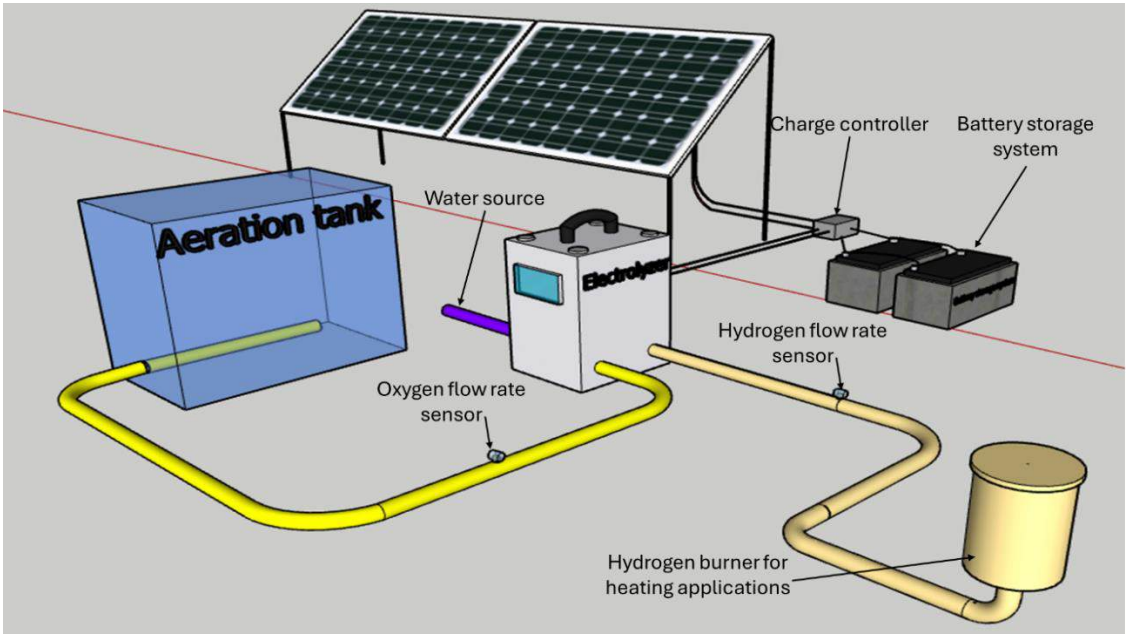

Figure 1. Schematic diagram of the experimental setup for green hydrogen production using PV modules, an electrolyzer, and a battery storage system.

This power is regulated through a charge controller to ensure stable operation and prevent overcharging of the connected battery storage system. The battery stores excess energy, providing a reliable power supply to the electrolyzer during periods of low solar availability. Water from a dedicated source is supplied to the electrolysis PEM unit, where it is split into hydrogen and oxygen gases. These gases are directed into a separation tank, where the oxygen and hydrogen are segregated. The hydrogen output is monitored via a flow rate sensor and sent to a burner for heating applications, demonstrating its practical use in thermal energy systems. Oxygen is also monitored and directed to an aeration tank to support secondary applications, such as enhanced oxygenation in water treatment processes. The hydrogen flow rate was measured using a Dwyer Visi-Float analog flow meter, with a measurement range of 0–5 L/min and an accuracy of ±3% of full scale, equivalent to approximately ±0.15 L for the 10-minute test duration. Oxygen was also produced at the anode during electrolysis and released into the atmosphere. Based on Faraday's law, the molar ratio of hydrogen to oxygen is 2:1. While oxygen was not quantitatively measured in this study, its generation was visually confirmed, and future system designs may include oxygen capture for utilization in secondary processes.

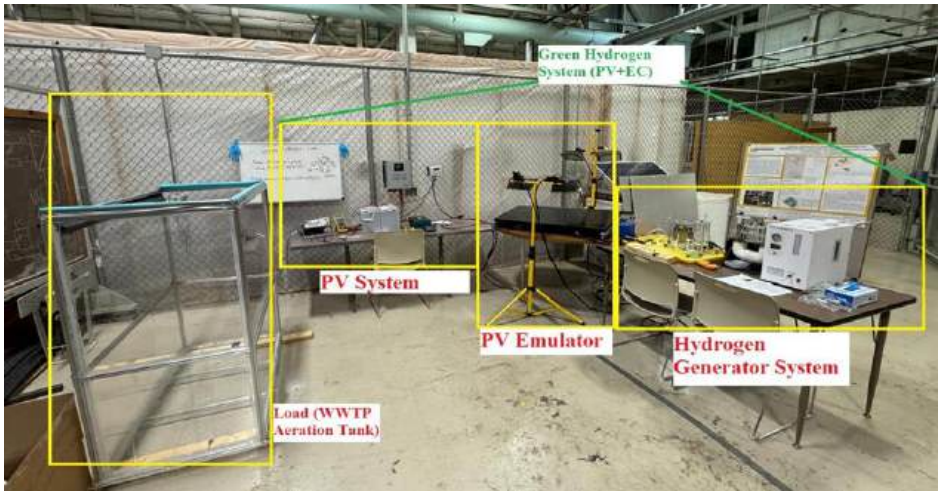

Figure 2. Prototype implementation of the experimental setup for hydrogen generation through solar-powered electrolysis.

To allow testing under varying conditions, a solar emulator simulates sunlight, ensuring flexible experimentation regardless of natural weather conditions. The data acquisition system includes a DataMaster Control Box and a power analyzer, which monitor power flow and log key performance metrics related to power output, system efficiency, and hydrogen production. The modular and scalable setup highlights the potential for integrating renewable energy sources with hydrogen production for future sustainable energy solutions.The implemented model and selected parameters are designed to match commercially available products to ensure practical and scalable deployment. To enhance data accuracy and ensure system safety, additional measuring instruments were integrated into the setup. A gas flow rate meter was used to quantify hydrogen production, offering a measurement range of 0–5 L/min and an accuracy of ±3%. Type K thermocouples were installed at key points to monitor temperature within a range of -50°C to 200°C, with an accuracy of ±1.1°C. A combustible gas leak detector was continuously used to detect potential hydrogen leaks, with a detection sensitivity of ≤50 ppm and a range up to 10,000 ppm. These devices were essential for validating experimental results and ensuring the safe operation of the system. The specifications of the key equipment used in the experimental setup are summarized in Table 1.

Table 1: Specifications of the Lab Components.

EQUIPMENT	SPECIFICATIONS
Battery	12V, 100Ah capacity, sealed lead-acid design
Charge Controller	12/24V, 30A capacity, regulates power from PV to storage system
Inverter	1000W, single-phase sine wave inverter, 12V input
Electrolyzer	200W, 12V, PEM
PV Panel	100W output, Vmp: 18.6V, Imp: 5.38A
Combustible Gas Leak Detector	Detection range: 0–10000 ppm; Sensitivity: ≤50 ppm

Gas Flow Rate Meter	Measures hydrogen output; Accuracy: ±3%; Range: 0–5 L/min
Temperature Sensors	Type K thermocouples; Accuracy: ±1.1°C; Range: -50°C to 200°C

B. Solar Emulator Design

The solar emulator in this experimental setup is designed to provide controlled and uniform light distribution to the PV panels, simulating solar irradiance conditions indoors. This emulator ensures that experimentation can be conducted irrespective of natural sunlight availability while accurately replicating real-world conditions. The design and optimization of the light distribution were achieved using simulation tools, allowing for precise adjustments and improved performance. The solar emulator consists of a series of high-intensity LED light strips strategically positioned above the PV panels. A photo of the implemented emulator showing the LED bar array and its mounting over the PV panel is provided in Figure 3. This setup demonstrates the physical arrangement used in the lab to deliver consistent and uniform irradiance. The LEDs are selected to emit light within the spectrum similar to sunlight, ensuring that the PV cells experience conditions that closely mimic actual outdoor irradiance. The physical arrangement of the LEDs and their spacing were optimized to minimize shading and achieve a uniform distribution of light across the PV panel surface.

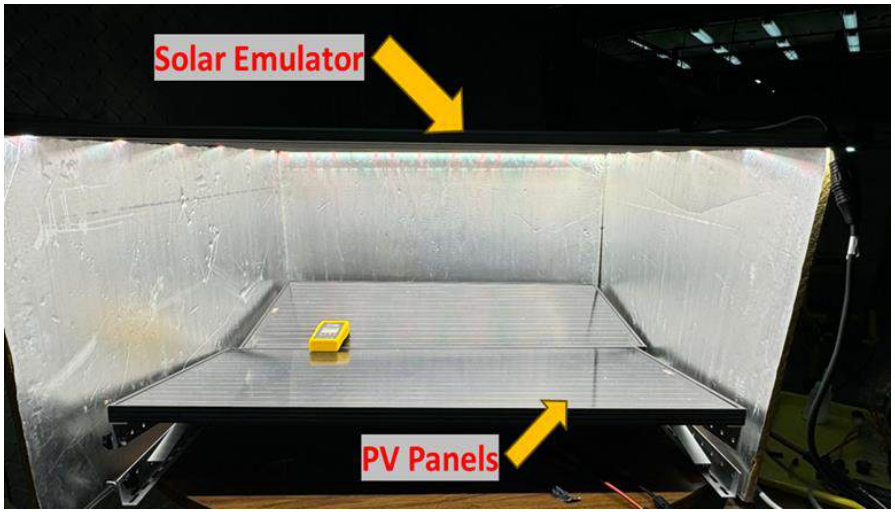

Figure 3: Solar emulator with LED light strips simulating solar irradiance for controlled PV panel testing

Each LED unit delivers up to 700 W of optical power and contains advanced horticultural-grade diodes with a spectral output tailored to match the 400–700 nm photosynthetically active radiation (PAR) range, aligning with the PV panel's peak spectral response. The fixture provides uniform light distribution over a 4 *ft* ×4 *ft* testing area, with dimmable intensity control and passive heat dissipation to maintain thermal stability during long-duration experiments.

To ensure that the emulator replicates natural sunlight conditions, irradiance distribution was modeled and optimized using simulation software. Measured I-V characteristics of the PV panel under emulator lighting were then compared to outdoor sunlight performance and benchmark data in literature. Results showed a deviation of less than 7%, validating the emulator's ability to deliver reliable and repeatable results under lab-controlled irradiance conditions. To validate and optimize the design, a computational simulation was performed using DIALux evo 9.2, a lighting simulation software commonly used for architectural lighting analysis [32]. The software provided a detailed irradiance contour map across the PV surface, enabling iterative refinement of the LED arrangement to achieve uniform intensity and eliminate hotspots or shadowed zones. The software

provided a detailed visual representation of how light is distributed, as shown in **Error! Reference source not found.**. The simulation considered factors such as panel angle, LED placement, and reflective surfaces within the emulator to ensure consistency. The software output included irradiance contour maps, as shown in **Error! Reference source not found.**, highlighting the intensity variations and guiding adjustments in the LED positioning to achieve near-uniform light coverage using DIALux software.

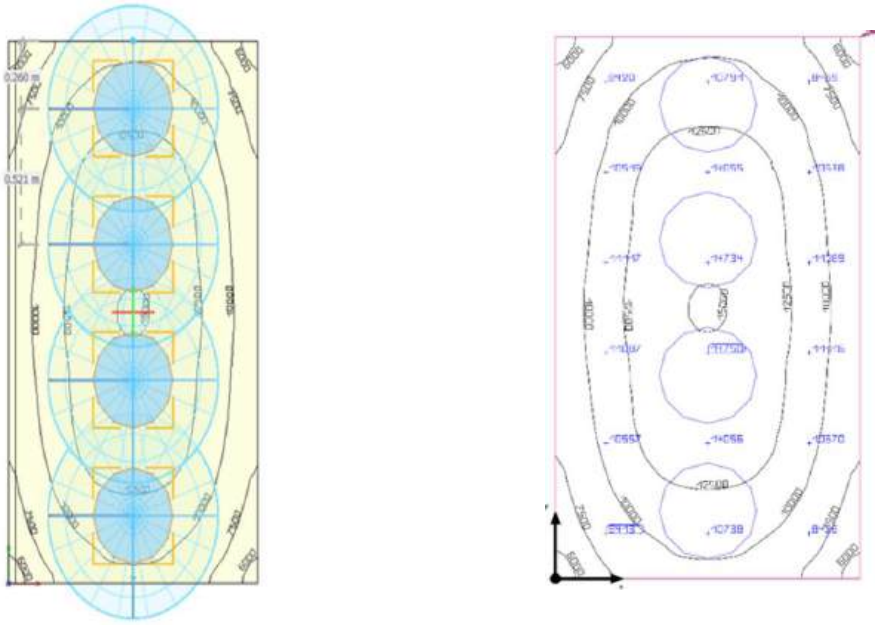

Figure 4: Simulated light distribution across the PV panel surface, showing optimized uniform irradiance.

The simulation also facilitated the identification and mitigation of hotspots and low-irradiance zones by iteratively refining the LED layout. Key parameters—such as LED mounting height, beam angle, spacing, and reflective boundaries—were systematically adjusted to optimize uniformity. This approach ensured that the irradiance across the PV panel surface was both consistent and closely matched typical outdoor solar conditions in terms of spatial distribution and spectral characteristics. As a result, the final design ensures that the PV panels receive consistent and sufficient irradiance, mimicking real solar conditions with high accuracy. This design not only improves the reliability of the experimental data but also ensures that the PV system's performance under varying light

conditions is accurately assessed, enhancing the overall precision of the hydrogen production experiments.

III. MATHEMATICAL MODELING

This section presents the mathematical modeling used to characterize the performance of a PV system integrated with an electrolyzer for hydrogen and oxygen production via water electrolysis.

A. Photovoltaic System Modeling

The electrical behavior of the PV system is described using fundamental equations and an equivalent circuit representation, Figure 5. The current output from the PV cell is expressed as Eq. 1:

$$I_{pv} = I_{ph} - I_d - I_{sh} \tag{1}$$

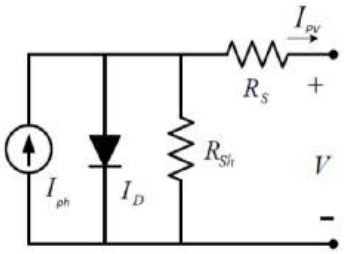

Figure 1: PV equivalent circuit

Eq. (1) describes that the output current (I_{pv}) is the difference between the photocurrent (I_{ph}), the diode current (I_d), and the shunt current (I_{sh}). The photocurrent depends on solar irradiance and temperature. I_d models current through the diode (p-n junction), and I_{sh} represents leakage losses due to cell imperfections.

The PV cell's equivalent circuit consists of a current source for I_{ph}, a diode, a series resistance (R_s) accounting for internal resistive losses, and a shunt resistance (R_{sh})

representing leakage across the junction. A more detailed expression for current under open-circuit conditions is given by Eq. (2):

$$I_{PV,0} = \frac{\left(I_{ph}(G,T) - \left[I_{ph}(G,T) - \left(\frac{VOC}{Rp}\right)\right] * \frac{e^{\frac{V}{Vt(T)*Ncs}}}{e^{\frac{VOC}{Vt(T)*Ncs}}} - \frac{V}{Rp}\right)}{1+\frac{Rs}{Rp}} \quad (2)$$

Eq. (2) comprehensively accounts for critical PV parameters including the open-circuit voltage (Voc), diode ideality factor (Ncs), thermal voltage (Vt), and the resistive components Rs and Rp. These parameters are essential for capturing the nonlinear electrical characteristics of photovoltaic cells under varying environmental conditions such as irradiance fluctuations and temperature changes. By integrating these factors into the model, the system provides a more robust and predictive simulation of PV behavior, which is indispensable for reliable energy output estimation.

The electrical power generated by the PV array serves as the input to the electrolyzer. Consequently, the current-voltage (I–V) profile of the PV system plays a pivotal role in determining the operational regime and efficiency of hydrogen production. The interaction between these two subsystems—PV and electrolyzer—is therefore central to the system's overall energy conversion efficiency and is rigorously characterized within this integrated framework.

B. Hydrogen Production Model

The model links the PV system's output to the electrolyzer's input through the relationship between electrical energy and gas production.

$$\mathrm{H_2} = \left[\frac{\mathrm{P \cdot V_{H_2}}}{\mathrm{R \cdot T}}\right] \times 1.67 \times 10^{-3} \quad (3)$$

Eq. (3) is derived from the Ideal Gas Law PV = nRT, estimates the quantity of hydrogen gas produced based on the pressure (P), volume (V), and temperature (T) within the

electrolyzer. The universal gas constant (R) where The universal gas constant was taken as R = 8.314 J/mol·K, and standard temperature and pressure (STP) conditions were assumed where applicable. In cases where molar volume was used directly, the value of 22.4 L/mol at STP was applied. All gas law-based calculations maintained unit consistency throughout., and a specific conversion factor 1.67×10^{-3} ,adjusts for non-ideal conditions in the electrolyzer, accounting for system losses and variations in gas behavior.

The electrochemical reaction for water splitting is given by Eq. (4):

$$2H_2O(l) \rightarrow 2H_2(g) + O_2(g) \quad (4)$$

This process is powered by renewable energy from the PV system and relies on precise control of current and voltage inputs to maximize the production efficiency of hydrogen and oxygen gases.

The mathematical model plays a critical role in predicting hydrogen production rates under various environmental conditions. By integrating real-time measurements of current, voltage, pressure, and temperature, the model refines the Ideal Gas Law using the unique conversion factor. This adjustment compensates for real-world discrepancies, such as energy losses in the system, electrolysis efficiency, and gas behavior at specific operating temperatures and pressures. Consequently, the model offers an accurate representation of the system's performance, ensuring reliable predictions of hydrogen output and supporting system optimization for sustainable green hydrogen production.

IV. RESULTS AND DISCUSSION

This section presents the findings from the comprehensive analysis of integrating PV systems with the aeration tanks of a WWTP. A series of power flow studies were conducted to evaluate the electrical performance under various operational scenarios, both with and without PV integration. Additionally, experimental assessments were performed to determine the impact of the aeration tanks on the efficiency of the PV panels. Uncertainty for each measurement was calculated based on equipment datasheets and is shown as error bars in the graphs to represent the confidence range in the experimental data. The following

subsections detail the outcomes of these studies, providing insights into the system's stability, energy efficiency, and the synergistic effects of combining PV technology with aeration processes.

A. I-V Characteristics of PV Modules under Variable Irradiance

The performance of the PV modules was characterized by their current-voltage (I-V) behavior under different irradiance levels, as illustrated in **Error! Reference source not found.**. The irradiance levels ranging from 101 W/m^2 to 265 W/m^2 were selected based on actual outdoor solar radiation measurements recorded in Milwaukee, Wisconsin, under cloudy and partially sunny winter conditions. These values were used in the emulator to replicate realistic sub-optimal solar scenarios, which are important for assessing system performance beyond ideal test conditions, and the experiments were conducted using the solar emulator to provide controlled, consistent testing conditions. The results reveal a strong dependence of the short-circuit current (I_{sc}) on the irradiance level, consistent with the theoretical relationship between photocurrent (I_{ph}) and solar radiation intensity. As expected, the short-circuit current (I_{sc}) increased linearly with rising irradiance, with the highest current output of approximately 2.5 A observed at 265 W/m^2. At lower irradiance levels, such as 101 W/m^2, the current output decreased significantly, confirming that the charge carrier generation within the PV cells is directly proportional to the photon flux incident on the cell. This trend aligns with the predictions of the PV cell equivalent circuit model, where I_{ph} dominates the output current under varying sunlight conditions.In contrast to the current response, the V_{oc} exhibited only a marginal increase with increasing irradiance, as the voltage depends more on the material properties of the PV cell and the temperature-dependent saturation current of the diode.

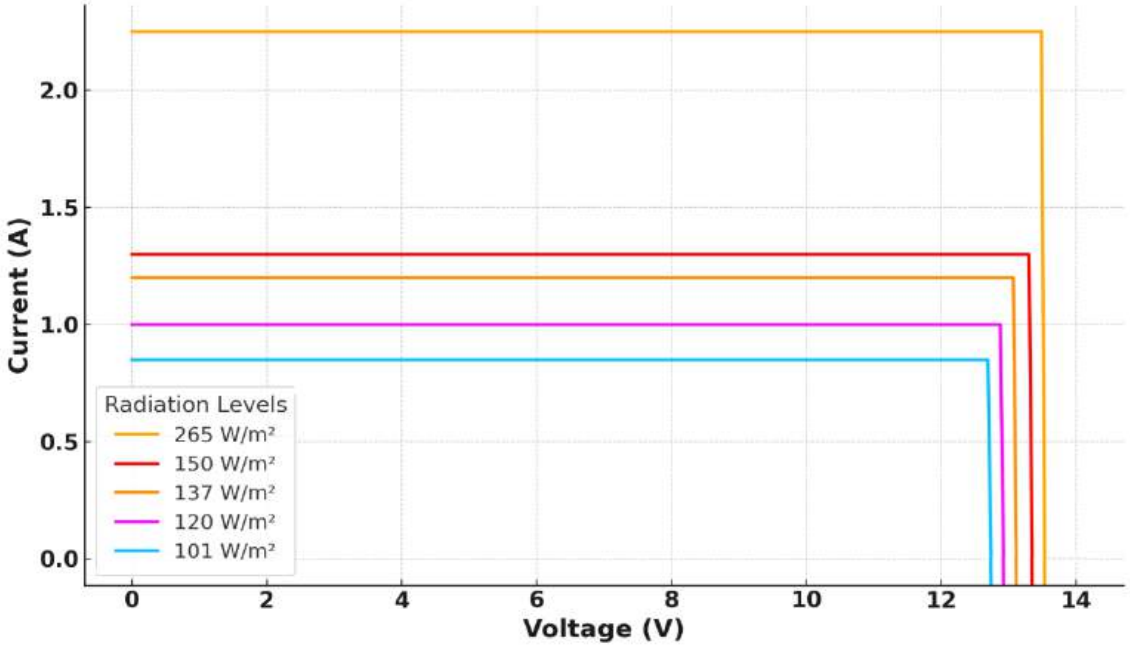

Figure 6. I-V characteristics of PV modules under varying irradiance

The observed variations in voltage were minimal, indicating that changes in irradiance primarily affect the current output rather than the voltage.The flat portions of the I-V curves, particularly at high irradiance levels, highlight the modules' ability to deliver a relatively stable current over a range of voltages, a critical attribute for ensuring reliable power supply to the electrolyzer. This characteristic enhances the stability of the electrolyzer's input power, mitigating fluctuations in the electrolysis process and supporting continuous hydrogen generation. The results from the I-V characteristics, Figure 6, demonstrate the effectiveness of the solar emulator in accurately simulating varying solar conditions and validate the capability of the PV system to meet the power requirements of the electrolyzer. These findings provide a foundation for further performance analysis by correlating the PV output to the electrolyzer's hydrogen production rates under different operating conditions. The observed data will be utilized in future work to optimize the integrated system and enhance overall efficiency through improved energy management strategies.

B. Electrolyzer Performance: I-V and P-V Characteristics

The performance evaluation of the electrolyzer was conducted using experimental data obtained from the implemented lab setup, as shown in **Error! Reference source not found.**. The applied voltage was varied from 0 to 8.5 V, and the resulting current and power outputs were measured in real-time to assess the electrolyzer's behavior and efficiency under operating conditions consistent with the PV system's power supply.

The experimentally measured I-V curve exhibits the characteristic nonlinear behavior of electrolytic processes. At low voltages (below approximately 1.8–2 V), the current remains near zero, indicating insufficient energy to overcome the activation barrier of the water-splitting reaction. In this region, minimal hydrogen production is observed due to limited electrochemical activity. As the voltage surpasses the threshold value of 2 V, a rapid increase in current occurs, reflecting the onset of significant hydrogen production. The current reaches approximately 1 A at 4 V and peaks at 2.5 A at 8.5 V. This sharp current rise demonstrates the accelerated electrolysis process once the activation energy requirement is met, with the current output strongly dependent on the applied voltage. The nonlinear growth in current emphasizes the importance of maintaining an appropriate voltage range to maximize hydrogen output efficiently.

The experimentally obtained P-V curve, which represents the power delivered to the electrolyzer as a function of the applied voltage, follows a quadratic trend consistent with the relationship $P=V\times I$. At low voltages (below 2 V), the power output is negligible due to minimal current flow. However, as the voltage increases beyond the activation threshold, the power rises rapidly, reaching a maximum of 21 W at 8.5 V. This result highlights the trade-off between energy input and hydrogen production rate. While higher voltages result in greater power delivery and hydrogen output, the increasing energy consumption due to resistive losses and overvoltage effects reduces the overall system efficiency. Therefore, identifying an optimal voltage range is critical to achieving efficient hydrogen production without excessive energy consumption.

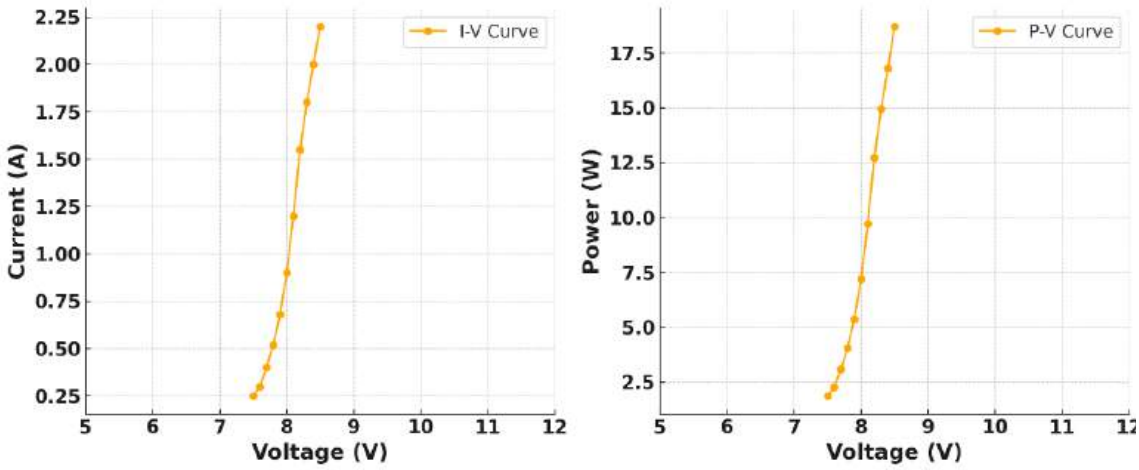

Figure 7. Experimentally measured I-V (left) and P-V (right) curves of the electrolyzer

The experimental results shows that the optimal operating voltage range for the electrolyzer is between 4.5 V and 7.5 V. Within this range, the electrolyzer achieves a high current output, ensuring substantial hydrogen production, while avoiding the significant efficiency losses associated with higher voltages. Operating beyond 8 V results in diminishing returns due to nonlinear power consumption and increased resistive heating. These findings, obtained directly from the implemented lab system, are crucial for integrating the PV system with the electrolyzer effectively. By dynamically adjusting the operating voltage based on the available solar power, the system can maximize hydrogen production while maintaining high energy efficiency.

C. Green Hydrogen Production

The relationship between the current supplied to the electrolyzer and The measured hydrogen volumes was normalized to time and presented as flow rates (L/min) for better clarity and standardization. This allows a more direct comparison of hydrogen production performance under varying current conditions as illustrated in In Figure 8, f. The data, collected directly from the implemented lab-scale setup, reveal a strong correlation between the supplied current and the rate of hydrogen generation. The setup consists of a PV system connected to the electrolyzer through a charge controller and battery storage to ensure stable power delivery. The current to the electrolyzer is adjusted to simulate varying

real-world solar power conditions and to evaluate the efficiency of hydrogen production under different operating currents. To ensure the reliability of experimental results, uncertainty bars have been included in all performance-related figures. These represent sensor accuracy as per manufacturer specifications. Hydrogen volume data includes an uncertainty of ±0.15 L, derived from the ±3% full-scale accuracy of the flow rate meter. Current and power readings include ±0.5% uncertainty, based on the power analyzer's datasheet.

At low current levels (0–0.5 A), hydrogen production is minimal, with less than 0.5 L generated during the 10-minute period. This corresponds to the initial activation phase of electrolysis, where most of the energy input is consumed in overcoming the activation energy needed for the water-splitting reaction. As the current increases beyond 0.5 A, hydrogen production exhibits a near-linear relationship, reaching approximately 3.0 L at a current of 2.5 A. This linear behavior is in accordance with Faraday's law of electrolysis, which states that the amount of hydrogen produced is proportional to the electric charge passed through the electrolyte.

The lab experiments confirmed this theoretical prediction by continuously monitoring hydrogen production using a gas flow meter and integrating the recorded flow rate over the 10-minute interval. The power supplied to the electrolyzer was dynamically controlled to maintain the desired current levels using real-time data from the power analyzer and the DataMaster control system, ensuring accurate measurements and system stability. The observed near-linear increase in hydrogen production suggests that the electrolyzer operates efficiently within the current range of 1.0–2.5 A. However, slight deviations from perfect linearity are seen at higher current levels, which are attributed to system inefficiencies such as increased resistive heating, gas bubble formation on the electrode surfaces, and limitations in ion transport within the electrolyte. These effects were also confirmed during lab observations, where excessive current resulted in localized heating and reduced hydrogen flow consistency.

The experimental setup highlights the importance of optimizing current density to balance hydrogen production rates and system efficiency. The integration of these results into the

PV-electrolyzer system ensures that the current can be dynamically adjusted based on real-time solar power availability. By maintaining the operating current within the optimal range, the system can achieve maximum hydrogen production while minimizing energy losses and inefficiencies.

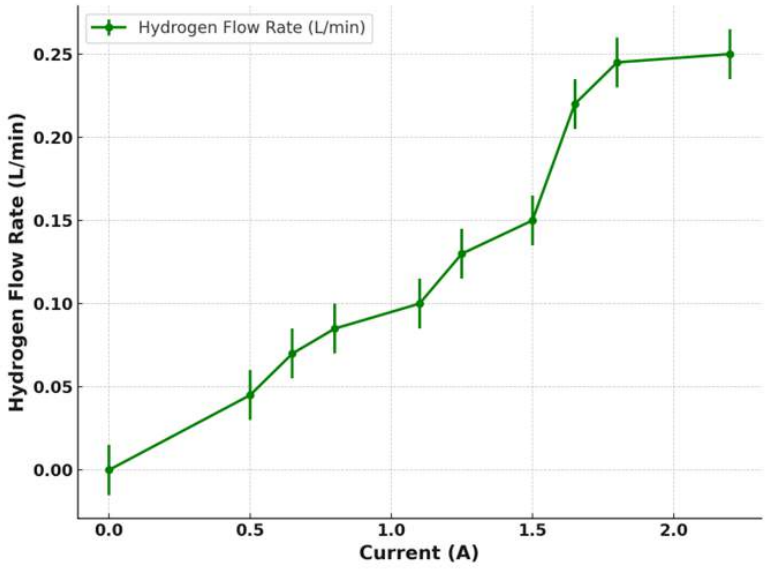

Figure 8. Hydrogen flow rate as a function of input current.

In Figure 8, f*low rates were calculated by dividing the total hydrogen volume collected over 10 minutes. Error bars represent ±0.015 L/min uncertainty based on ±3% full-scale accuracy of the flow sensor.* To further validate the system's efficiency, Figure 9 shows a correlation between hydrogen produced (liter) and input electrical energy (Watt-minute) presents the relationship between input electrical energy and the amount of hydrogen produced. As shown, a near-linear correlation is observed, confirming that higher electrical energy results in greater hydrogen output, in line with Faraday's Law.

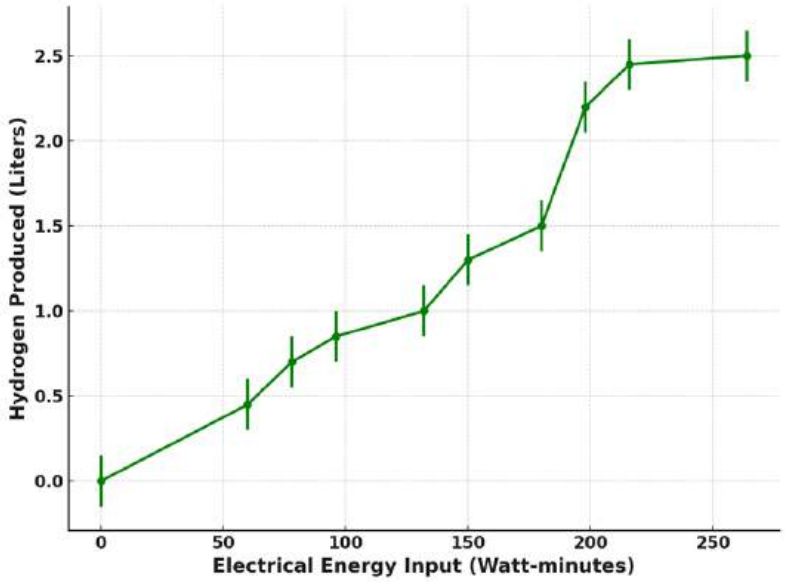

Figure 9. Correlation between hydrogen produced and input electrical energy

This graphical representation supports the system's classification as an efficient hydrogen production platform. Figure 9 shows a correlation between hydrogen produced (liter) and input electrical energy (Watt-minute) over a 10-minute interval. The error bars represent ±0.15 L hydrogen flow uncertainty.

V. CONCLUSIONS

This paper presents a novel lab-scale system for green hydrogen production by PV modules, advanced power electronics, and an electrolyzer. The implemented system system addresses critical challenges associated with system efficiency, scalability, and the intermittent nature of solar energy. A key innovation of this study is the design and implementation of a solar emulator, enabling controlled experiments under varying irradiance conditions and ensuring reliable performance evaluation. By dynamically optimizing power delivery from the PV system to the electrolyzer through real-time monitoring and control, the system achieved stable hydrogen production with minimal efficiency losses. The experimental results demonstrate that operating the electrolyzer within an optimal current range of 1.0–2.5 A leads to efficient hydrogen production, with

up to 3.0 L of hydrogen generated over a 10-minute operational period. The I-V and P-V characteristics reveal that an optimal voltage range of 4.5–7.5 V effectively balances hydrogen production rates while minimizing resistive and overvoltage losses. The integration of a charge controller and battery storage system further supports stable power delivery, allowing continuous operation under fluctuating solar conditions. This modular and scalable design shows significant potential for practical deployment in industrial and transportation applications, contributing to decarbonization and environmental sustainability. Future work will focus on optimizing the electrolyzer's performance through advanced electrode design, improved catalysts, and optimized electrolyte flow to minimize resistive losses and enhance reaction efficiency. Intelligent power management systems will be developed to dynamically adjust power allocation based on real-time solar conditions, ensuring consistent hydrogen production. Additionally, heat management and recovery mechanisms will be explored to improve long-term system stability and efficiency. Scaling the system to pilot and industrial levels will be prioritized, with integration into microgrid networks and hybrid renewable energy systems.

ACKNOWLEDGMENTS

The US Department of Energy (DoE) funds the research under the DE-EE0009728 grant.

NOMENCLATURE

I_{pv}	Output current of the photovoltaic cell
I_{ph}	Photocurrent generated by incident light
I_d	Diode current
I_{sh}	Shunt current
R_s	Series resistance of the PV cell
R_{sh}	Shunt resistance of the PV cell
V_{cell}	Voltage across the PV cell
V_{OC}	Open-circuit voltage of the PV cell
V_t	Thermal voltage
N_{cs}	Ideality factor of the diode Ncs
P	Pressure of hydrogen gas
V_{H2}	Volume of hydrogen produced
R	Universal gas constant
T	Temperature during electrolysis
I_{sc}	Short-circuit current of the PV module
P_{max}	Maximum power delivered to the electrolyzer

H_2	Hydrogen gas output

REFERENCES

1. International Energy Agency (IEA), "Solar PV Global Analysis," 2023.
2. National Renewable Energy Laboratory (NREL), "Photovoltaic Research," 2023.
3. A. M. Aly, "Breaking Boundaries in Wind Engineering: LSU WISE Open-Jet Facility Revolutionizes Solar Panel and Building Design," Applied Sciences, vol. 13, p. 12546, 2023. [Online]. Available: https://doi.org/10.3390/app132312546
4. T. Xue, Y. Wan, Z. Huang, P. Chen, J. Lin, W. Chen, and H. Liu, "A Comprehensive Review of the Applications of Hybrid Evaporative Cooling and Solar Energy Source Systems," Sustainability, vol. 15, p. 16907, 2023. [Online]. Available: https://doi.org/10.3390/su152416907
5. A. Sahu, N. Yadav, and K. Sudhakar, "Floating Solar Photovoltaic Systems: An Overview and Their Feasibility at Various Locations Worldwide," Renewable and Sustainable Energy Reviews, 2021.
6. M. Heinrich, C. Kutter, F. Basler, M. Mittag, L. Alanis, D. Eberlein, et al., "Potential and Challenges of Vehicle-Integrated Photovoltaics for Passenger Cars," Proc. of the European Photovoltaic Solar Energy Conf. and Exhibition (EU PVSEC), 2020. [Online]. Available: https://doi.org/10.4229/EUPVSEC20202020-6DO.11.1
7. M. Dada and P. Popoola, "Recent Advances in Solar Photovoltaic Materials and Systems for Energy Storage Applications: A Review," Beni-Suef Univ. J. Basic Appl. Sci., vol. 12, p. 66, 2023. [Online]. Available: https://doi.org/10.1186/s43088-023-00405-5
8. A. Aslam, N. Ahmed, S. A. Qureshi, M. Assadi, and N. Ahmed, "Advances in Solar PV Systems: A Comprehensive Review of PV Performance, Influencing Factors, and Mitigation Techniques," Energies, vol. 15, p. 7595, 2022. [Online]. Available: https://doi.org/10.3390/en15207595

9. R. Gupta and K. T. Chaturvedi, "Adaptive Energy Management of Big Data Analytics in Smart Grids," Energies, vol. 16, p. 6016, 2023. [Online]. Available: https://doi.org/10.3390/en16166016
10. UN Environment Programme, "Global Trends in Renewable Energy Investment," 2022.
11. A. Mondal and G. Wang, "Energy Storage Technologies for Solar Photovoltaic Systems," 2016. [Online]. Available: https://doi.org/10.1007/978-3-662-50521-2_9
12. International Energy Agency (IEA), "The Future of Solar Transportation Systems," 2021.
13. M. Heinrich et al., "Potential and Challenges of Vehicle-Integrated Photovoltaics for Passenger Cars," Proc. of the European Photovoltaic Solar Energy Conf. and Exhibition (EU PVSEC), 2020. [Online]. Available: https://doi.org/10.4229/EUPVSEC20202020-6DO.11.1
14. National Renewable Energy Laboratory (NREL), "Solar-Powered Public Transit Systems: A Case Study," 2023.
15. T. Xue, Y. Wan, Z. Huang, P. Chen, J. Lin, W. Chen, and H. Liu, "A Comprehensive Review of the Applications of Hybrid Evaporative Cooling and Solar Energy Source Systems," Sustainability, vol. 15, p. 16907, 2023. [Online]. Available: https://doi.org/10.3390/su152416907
16. A. Sahu, N. Yadav, and K. Sudhakar, "Solar Parks: Large-Scale PV Applications for Industrial Energy Demand," Renewable and Sustainable Energy Reviews, 2021.
17. International Renewable Energy Agency (IRENA), "Green Hydrogen: A Key to a Sustainable Future," 2021.
18. Johnson, P. and Liu, X., "Advances in PEM and Alkaline Electrolyzers for Green Hydrogen," Electrochemical Reviews, 2023.
19. National Renewable Energy Laboratory (NREL), "Improving Electrolyzer Longevity for Large-Scale Applications," 2023.
20. European Commission, "A Hydrogen Strategy for a Climate-Neutral Europe," 2020.

21. Y. Chen et al., "Hydrogen Storage Solutions: Challenges and Innovations," Energy Storage Materials, vol. 9, 2022.
22. P. Wang and K. Zhang, "Hydrogen Infrastructure and Integration Challenges," Energy Policy Journal, vol. 11, pp. 567-579, 2022.
23. National Research Council, "The Future of Green Hydrogen in Heavy-Duty Transport," 2022.
24. K. Müller et al., "Green Hydrogen Applications in Steel Manufacturing," Industrial Decarbonization, vol. 8, 2023.
25. Mondal, A. and Wang, G., "Renewable Integration for Hydrogen Scalability," Sustainable Energy Reviews, 2024.
26. J. Zhang et al., "High-performance capillary-fed electrolysis cell for green hydrogen production," Nature Communications, vol. 14, no. 2142, 2023.
27. L. Wang, M. Zhou, et al., "Membrane-based seawater electrolysis for hydrogen production," Nature, 2023.National Renewable Energy Laboratory, "U.S. Solar Photovoltaic System and Energy Storage Cost Benchmark: Q1 2020," Oct. 2020. [Online]. Available: https://www.nrel.gov/docs/fy21osti/77324.pdf. Accessed: Nov. 9, 2024.
28. Z. Liu, H. Wang, and Y. Li, "Fully Renewable Microgrids for Hydrogen Production: Integration with Battery Storage Systems," Electronics, vol. 13, no. 20, 2023. [Online]. Available: https://www.mdpi.com/2079-9292/13/20/3995
29. J. Smith, T. Kim, and R. Gupta, "Decentralized Control for Microgrid-Based Green Hydrogen Production Using PV Emulators," Oxford Research Archive, 2023. [Online]. Available: https://ora.ox.ac.uk/objects/uuid%3A8539e275
30. P. Wang et al., "Lab-Scale Experiments in PV-Integrated Microgrids for Hydrogen Production," arXiv preprint, 2024. [Online]. Available: https://arxiv.org/abs/2406.00597
31. Y. Chen and L. Zhou, "Modular Solutions for Scalable Microgrid-Integrated Electrolysis," arXiv preprint, 2023. [Online]. Available: https://arxiv.org/abs/2311.13149.

32. DIAL GmbH, *DIALux evo 9.2 [Computer software]*. Lüdenscheid, Germany: DIAL GmbH, 2023. [Online]. Available: https://www.dialux.com/en-GB/dialux

Author Biographies

Hamza Alnawafah, Ph.D., CEM®, NABCEP®, is an Energy Engineer at the U.S. Department of Energy Industrial Assessment Center. He is currently a Ph.D. candidate in Mechanical Engineering at the University of Wisconsin-Milwaukee. He holds a Ph.D. in Sustainable and Renewable Electrical Technologies. His research interests include renewable energy systems, smart grids, green hydrogen production, energy efficiency, power systems, automation, and control systems.

Qais Alnawafah, M.Sc., Ph.D. candidate, Research Assistant, Department of Mechanical Engineering, UWM. He has industrial experience as a mechanical engineer in renewable energy, energy auditing, manufacturing, and building maintenance. He has two years of experience in solar panels installation and testing.

Omar Alsotary is a Ph.D. student in Mechanical Engineering at the University of Wisconsin-Milwaukee and an energy engineer with the Industrial Training and Assessment Center (ITAC), where he conducts energy assessments for small and medium-sized manufacturers across the Midwest. Holding a master's degree in Environmental and Renewable Energy Engineering, his

expertise lies in enhancing energy efficiency for the HVAC and Heat Pump systems.

Ryo Amano is Richard & Joanne Grigg Fellow Professor and Director of the UWM-DOE Industrial Assessment Center at the University of Wisconsin-Milwaukee, who has been engaged in research on energy and aerospace subjects. The specific research areas that he has worked on include turbulence, aerospace study, renewable energy on the wind, hydro, and biomass, gas turbine.